# Supramolecular organization and biological interaction of the squalenoyl siRNA nanoparticles

Marie Caillaud, Frédéric Gobeaux, Miryana Hémadi, Suzan Boutary, Patrick Guenoun, Didier Desmaële, Patrick Couvreur, Frank Wien, Fabienne Testard, Liliane Massaad-Massade

# Supramolecular organization and biological interaction of ~~the~~ squalenoyl siRNA nanoparticles

Marie Caillaud,[1] Frédéric Gobeaux[2], Miryana Hémadi[3], Suzan Boutary[1], Patrick Guenoun[2], Didier Desmaële[4], Patrick Couvreur[4], Frank Wien[5], Fabienne Testard [2]and, Liliane Massaad-Massade[1]

[1] U1195 Diseases and Hormones of the Nervous System, INSERM U1195 and University Paris-Saclay, 94276, Le Kremlin-Bicêtre, France.

[2] LIONS - NIMBE CEA, CNRS, Université Paris-Saclay, CEA Saclay, 91191 Gif-sur-Yvette Cedex, France.

[3] Université de Paris, CNRS-UMR 7086, Interfaces, Traitements, Organisation et DYnamique des Systèmes (ITODYS), UFR de Chimie 75013 Paris, France.

[4] Institut Galien Paris-Sud, CNRS UMR 8612, Université Paris-Sud, Université Paris-Saclay, 92290 Châtenay-Malabry, France.

[5]SOLEIL Synchrotron, Saint Aubin, France.

***Corresponding author**: Liliane Massade, PhD, INSERM U1195, 94276 Le Kremlin-Bicêtre, France. Email: liliane.massade@inserm.fr, Phone: + 33 1 49 59 18 30

**Funding:** This work is supported by a public grant overseen by the French National Research Agency (ANR) as part of the "Investissements d'Avenir" program (Labex NanoSaclay, reference: ANR-10-LABX-0035).

**Key words**: siRNA, nanotechnologies, structural studies, biological interaction

**Chemical keywords**: Azido-Squalene ($N_3$-SQ), cationic squalenaldehyde hydrazinoguanidinium acetate salt ($SQ^+$), dibenzylcyclooctyne (DBCO), N-(hexamethylenyl)-6-oxohexanamide spacer (C6), Bovine serum albumin (BSA), Low density lipoprotein (LDL), Lipofectamine 3:1 DOSPA (2,3- dioleoyloxy- N-[2(sperminecarboxamido)ethyl]- N,N- dimethyl- 1- propaniminium trifluoroacetate) : DOPE (1,2-dioléoyl-sn-glycéro-3-phosphoéthanolamine), Sybr Green $C_{32}H_{37}N_4S$

Table of contents

## Abstract

Small interfering RNAs (siRNA) are attractive and powerful tools to inhibit the expression of a targeted gene. However, their extreme hydrophilicities combined with a negative charge and short plasma half-life counteract their use as therapeutics. Previously, we chemically linked siRNA to squalene (SQ) which self-assembled as nanoparticles (NPs) with pharmacological efficiency in cancers and recently in a hereditary neuropathy. In order to understand the siRNA-SQ NP assembly and fate once intravenously injected, the present study detailed characterization of siRNA-SQ NP structure and its interaction with serum components.

We discovered that the siRNA-SQ bioconjugate self-assembled as 11-nm diameter core/shell supramolecular assemblies, which are connected one to another to form spherical nanoparticles of around 130-nm diameter. The siRNA-SQ NPs were stable in biological media and interacted with serum components, notably with albumin and LDL. The high specificity of siRNA to decrease or normalize gene expression and the high colloidal stability when encapsulated into squalene nanoparticles offer promising targeted therapy with wide applications for pathologies with gene expression dysregulation.


## 1. Introduction

Small interfering RNAs (siRNA) discovered by Fire and Mello at the end of the 90s (Fire, Xu et al. 1998), are small double-stranded RNAs composed of 19-21 bases pairs with 3'-cohesive ends. The antisense strand is complementary to a targeted messenger RNA (mRNA), leading to its degradation and gene silencing (Elbashir 2001, Elbashir, Martinez et al. 2001). Despite their specificity and efficiency at low doses, their intrinsic parameters constitute the main hurdles for *in vivo* delivery (Caillaud, El Madani et al. 2020). Indeed, in blood, naked siRNAs are rapidly degraded by nucleases and cleared by glomerular filtration, resulting in short plasmatic half-life (less than 15 mins) (Thompson, Kornbrust et al. 2012, Ozpolat, Sood et al. 2014). Moreover, their hydrophilic and polyanionic nature prevents efficient cellular uptake (Whitehead, Langer et al. 2009, Kanasty, Dorkin et al. 2013).

We previously developed an original approach for the conjugation of siRNA to squalene (SQ), a precursor of the cholesterol's biosynthesis. The so-called "Squalenoylation" technology consists of the bioconjugation of this lipid to a biologically active molecule, adopting a compact molecular conformation in aqueous media (Couvreur, Stella et al. 2006,

Couvreur, Reddy et al. 2008, Desmaele, Gref et al. 2012). Squalene was initially covalently coupled to siRNA *via* maleimide-sulfhydryl chemistry and the resulting siRNA-SQ nanoparticles (siRNA-SQ NPs) showed significant results in reducing tumor growth in two cancer models with fusion oncogenes: RET/PTC1 and RET/PTC3 (present in papillary thyroid carcinoma) and TMPRSS2-ERG (found in prostate cancer) (Raouane, Desmaele et al. 2011, Ali, Maksimenko et al. 2014, Ali, Urbinati et al. 2014, Urbinati, Ali et al. 2015, Urbinati, de Waziers et al. 2016). The conjugation method has been further improved, implementing strain-promoted azide-alkyne cycloaddition. This copper-free (Cu-free) click chemistry approach increased the bioconjugation yield while preserving the antineoplastic activity of siRNA TMPRSS2-ERG-SQ NPs in a xenografted cancer model (Massaad-Massade, Boutary et al. 2018). Recently, we succeeded in delivering squalenoyl siRNA targeting PMP22, an overexpressed gene causing hereditary neuropathy, *i.e.* the Charcot-Marie-Tooth 1A (CMT1A) disease. The intravenous administration of siRNA PMP22-SQ NPs restored both motor and neuromuscular activities in transgenic mouse models (Boutary, Caillaud et al. 2021). Moreover, the targeted gene expression normalization indicated that the NPs successfully entered into the targeted tissue, the sciatic nerve and more specifically inside Schwann cells.

To better understand the siRNA-SQ NPs fate, their structure, as well as their biological behavior once intravenously injected into the circulating bloodstream should be investigated. Indeed, characterization of size, shape, surface properties and structure of siRNA-SQ NPs is important because these parameters may dramatically affect their biological outcome such as tissue accumulation and cell uptake (Kang, Kim et al. 2016, Dormont, Rouquette et al. 2019). In our previous studies, basic physicochemical parameters, like overall size and surface charge, were determined. However, their supramolecular organization, another key issue for the therapeutic efficiency in terms of availability and release of the active molecule (Lepeltier, Bourgaux et al. 2014, Kang, Kim et al. 2016), had never been investigated. Therefore, in the present study, high-resolution small-angle scattering has been performed to obtain new insights on the supramolecular organization of these nanoparticles.

*In vivo* interactions of nanoparticles with blood components represent another key point for biomedical applications. The interaction with serum biomolecules has already been investigated with squalenoyl conjugates bearing a small active functional group, like gemcitabine, doxorubicin (Sobot, Mura et al. 2017, Sobot, Mura et al. 2017, Yesylevskyy, Ramseyer et al. 2018) or adenosine (Gobeaux, Bizeau et al. 2020) but, never so far with macromolecules such as siRNA. Consequently, understanding the interaction between

siRNA-SQ NPs and blood proteins is mandatory for further development towards clinical applications. Among serum components interacting with NPs, we have focused our attention on albumin and lipoproteins (LPs).

Albumin is the most abundant serum protein (55%) and acts as carrier for several other endogenous proteins, such as steroids and fatty acids (Sleep 2015, Mariam, Sivakami et al. 2016, Lamichhane and Lee 2020). Human albumin has been investigated and approved in clinics to deliver paclitaxel, a chemotherapy drug, to cancer cells (Abraxane®) or to extend the plasmatic half-life of insulin hormone linked to a fatty acid (Levemir®), which allows for 98% binding to this protein (Kratz 2008). On the other hand, lipoproteins (LPs) are the third most abundant plasma molecules in humans. They consist of an assembly of lipids and proteins. Low-density lipoproteins (LDL) are the main carriers for cholesterol (75%) and fatty acids in mammals (Schumaker and Adams 1969). Thanks to their apolipoproteins (amphiphilic protein) embedded in the outer membrane, LPs bind to lipoprotein receptors resulting in cellular uptake by clathrin-mediated endocytosis (Chaudhary, Bower et al. 2019). These macromolecules interact in the bloodstream with lipophilic drugs and deliver them to tissues, such as the liver and tumors (Wolfrum, Shi et al. 2007, Wasan, Brocks et al. 2008, Chaudhary, Bower et al. 2019).

In the present study, we first fully characterized the external and internal structure of siRNA-SQ NPs at the supramolecular level and we assessed the interactions between siRNA-SQ NPs and serum components, notably albumin and LDL.

## 2. Materials and Methods

### 2.1. Chemicals

All chemicals used were of highest analytical grade and purchased from Sigma–Aldrich. The anhydrous solvents were dried and distilled before use (tetrahydrofuran (THF) on Na/benzophenone) and reactions sensitive to air or humidity were performed under nitrogen pressure. $D_2O$ (99.85% D) for small angle neutron scattering (SANS) experiments was purchased from Eurisotop (France).

Modified siRNAs for the Cu-free click chemistry reactions were purchased from Eurogentec (France). Azido-Squalene and cationic squalenaldehyde hydrazinoguanidinium acetate salt ($SQ^+$) were synthetized according to our previous studies (Bertrand, Lucas et al. 2015, Massaad-Massade, Boutary et al. 2018). Dulbecco's modified Eagle medium (DMEM), Opti-MEM, fetal bovine serum (FBS) were purchased from Fisher Scientific (Illkirch, France). UltraPure™ distilled water (Dnase and Rnase free water) purchased from Invitrogen. Water was purified using a Milli-Q system.

LDLs from human plasma [dissolved in 10 mM Tris, 150 mM NaCl, 0.3 mM EDTA pH 8.3 and 2 mM $NaN_3$] were purchased from Invitrogen (Thermo Fisher Scientific). For small-angle scattering and fluorescence experiments, lyophilized BSA powder was dissolved to a 200 µM concentration in 0.2 M Phosphate Buffer Saline (PBS) then in $H_2O$ for standard experiments and in $D_2O$ for SANS experiments. BSA solutions were dialyzed overnight against at least a 10-fold volume PBS/$D_2O$ (or PBS/$H_2O$) solution, then stored at 4 °C. FBS was also dialyzed overnight against PBS/$D_2O$ just after bottle opening.

### 2.2. siRNAs used and chemical modifications

The siRNA targeting RET/PTC1 and PMP22 used in the experiments were previously described (Ali, Maksimenko et al. 2014, Massaad-Massade, Boutary et al. 2018, Boutary, Caillaud et al. 2021). All single-stranded RNAs were synthesized by Eurogentec (France) and purified by RP-HPLC. Single-strand RNAs were synthesized as 19-mers with two 3′-overhanging 2′-deoxynucleotide residues to provide stabilization against nucleases, as described by Tuschl *et al.* (Tuschl 2002). To allow conjugation with squalene, a dibenzocyclooctyne (DBCO) reactive group and a linker N-(hexamethylenyl)-6-oxohexanamide spacer (C6) were introduced at the 5′-end of the sense strand of each siRNA (Massaad-Massade, Boutary et al. 2018).

To anneal naked siRNA (*i.e.* siRNA not coupled to SQ), equimolar amounts of sense and antisense strands were mixed with the hybridization buffer [30 mM HEPES-KOH (pH 7.4), 2 mM Mg acetate, 100 mM K acetate]. The mixture was incubated for 3 min at 95°C and then for 45 min at room temperature before being stored at -80°C.

### 2.3.Preparation of siRNA-SQ nanoparticles

Cu-free click chemistry, a 1,3–dipolar cycloaddition was developed by our lab as previously described (Massaad-Massade, Boutary et al. 2018, Boutary, Caillaud et al. 2021). Then, the siRNA-SQ NPs were prepared by inverse nanoprecipitation in acetone/water as sketched in Figure S1. Practically, annealed siRNA-SQ bioconjugates in UltraPure$^{TM}$ distilled water (Dnase and Rnase free water) were added drop wisely to a stirred organic phase (acetone) with a volume/volume ratio of 1 [organic phase]: 2 [aqueous phase]. Then acetone was evaporated using nitrogen flux for 30 min to obtain an aqueous suspension of pure siRNA-SQ NPs.

### 2.4. Physicochemical characterization of siRNA-SQ nanoparticles

Hydrodynamic diameter, PDI and ζ-potential were measured by dynamic light scattering (DLS) using the Malvern Zetasizer Nano ZSP (Malvern Instrument) with a scattering angle of 173° for size measurements. Samples were analyzed at 10 µM concentration in RNase-free water.

Cryogenic Transmission Electron Microscopy (cryo-TEM) was performed with a JEOL 2100 electron microscope at the Electronic Microscopy Platform (IBPS/Institut de Biologie Paris-Seine, Université P. et M. Curie, Paris, France). A 4 µL drop of the concentrated siRNA-SQ NPs (166 µM) was deposited on a carbon-coated copper grid. Excess liquid was removed with blotting filter paper, and the samples were quickly vitrified by plunging them into liquid ethane using a guillotine-like frame. The samples were then transferred to a cryo-sample holder. Observations were made at an acceleration voltage of 200 kV under a low electron dose. Analysis was performed with Image J software.

### 2.5. Preparation of siRNA-SQ/SQ$^+$ NPs

Cationic squalenaldehyde hydrazinoguanidinium acetate salt ($SQ^+$) was dissolved in acetone at a concentration of 1 mg/mL and added dropwisely to a suspension of already prepared siRNA-SQ NPs at a molar ratio of 1 [NPs]:100 [$SQ^+$]. The organic solvent was then

evaporated for 30 min under stirring using the nitrogen flow to obtain siRNA-SQ/$SQ^+$ NPs in aqueous solution. Then size and ζ-potential were measured.

### 2.6. Cell lines and culture

BHP 10-3 is a papillary thyroid carcinoma cell line harboring the fusion oncogene *RET/PTC1* and MSC80 is a mouse Schwann cell line expressing *PMP22*. Both cell lines were maintained at 37 °C in an atmosphere of 5% $CO_2$ and 95% humidity in complete DMEM supplemented with 10% heat-inactivated FBS, with 100 units/mL penicillin, and 100 µg/mL streptomycin.

### 2.7. *In vitro* cell transfection

One feature of siRNA-SQ NPs is that they cannot spontaneously enter into cells *in vitro* without the help of a transfection agent (Raouane, Desmaele et al. 2011, Ali, Maksimenko et al. 2014, Urbinati, Ali et al. 2015, Massaad-Massade, Boutary et al. 2018, Boutary, Caillaud et al. 2021). Therefore, Lipofectamine 2000 was used to assess naked siRNA and siRNA-SQ NPs efficiency *in vitro*.

To study the effect of surface charge, 3 x $10^5$ cells of BHP 10-3 and MSC80 were seeded, 24 h before transfection, in six-well plates in DMEM supplemented with 10% FBS, penicillin (100 U/mL), and streptomycin (10 µg/mL). The next day, the cell medium was replaced with 2mL of Opti-MEM medium (Gibco Life technologies, ref. 11058021). The siRNA-SQ NPs and naked siRNA were transfected using Lipofectamine 2000, according to the supplier's recommendations, in the reduced Opti-MEM medium for a final concentration of 50 nM/well. Similarly, siRNA-SQ/$SQ^+$ NPs and siRNA-SQ NPs alone (as a negative control) were added to Opti-MEM and incubated with the cells. 4h later, the medium was replaced by complete DMEM and 48 h later the experiments were stopped, and RNA was extracted to analyze silencing of targeted genes *RET/PTC1* and *PMP22*. Each experiment was performed at least twice in duplicate.

### 2.8. mRNA Extraction and Real-Time PCR (RT-qPCR) experiments

Total RNA was extracted from BHP 10-3 and MSC80 cells using the RNeasy mini-kit (Qiagen, Courtaboeuf, France). Reverse transcription was performed using the M-MLV RT buffer pack (Invitrogen, Charbonnières-les-Bains, France). Then, real-time PCR (qPCR) was carried out with the CFX96TM Real-time system (Biorad) using the Maxima Syber Green Rox qPCR master Mix (Thermo Scientific, Villebon-sur-Yvette, France), according to the manufacturer's instructions. Samples were run in duplicate; gene expression was determined

by the $2^{-\Delta\Delta Ct}$ method. Relative mRNA levels of targeted genes (*RET/PTC1* and *PMP22*) were compared to non-treated (NT) cells after normalization regarding control gene levels in at least 2 independent experiments.

### 2.9. Small-Angle Neutron Scattering (SANS)

SANS experiments were carried out on the D33 spectrometer at ILL (doi: 10.5291/ILL-DATA.9-13-781). Samples prepared in $D_2O$ were placed in 1-mm size Hellma quartz cells and thermostated at 20°C. The raw data were radially averaged, corrected for electronic background and normalized by water scattering using the LAMP software (Richard, Ferrand et al. 1996). Three configurations were used to cover a *q* range going from 0.0013 to 0.27 $Å^{-1}$: 1) wavelength: $\lambda$ = 13 Å, sample detector distance D = 12 m, collimation: $\Phi$ = 12.8, 2) $\lambda$ = 4.6 Å, D = 12 m, collimation: $\Phi$ = 7.8 and 3) $\lambda$ = 4.6 Å, D = 2 m, collimation $\Phi$ = 7.8, for small, medium and large angles, respectively.

### 2.10. Small-Angle X-ray Scattering (SAXS)

Small-angle X-ray scattering patterns (SAXS) were obtained on the SWING beamline of the SOLEIL synchrotron (Saint-Aubin, France). The scattering vector range *q* of $2\times10^{-3}$ $Å^{-1}$ to 2.5 $Å^{-1}$ was obtained with an energy of 16 keV and two sample-to-detector distances (6 and 0.50 m for the SAXS and the wide-angle X-ray scattering ranges, respectively). The data were recorded by a two-dimensional Eiger 4M (Dectris) detector. Data reduction was performed using Foxtrot software, an application developed at SOLEIL. The sample was placed in a 1.5-mm diameter quartz capillary sealed with kerosene wax.

### 2.11. siRNA-SQ NPs internal structure characterization

Analysis of the SANS and SAXS patterns of siRNA PMP22-SQ NPs in aqueous solution allows to draw a first sketch of the shape and internal structure of the NPs. The scattering curves were fitted by SASview software (www.sasview.org/) to a lognormal sphere distribution model for the siRNA-SQ particles and a cylinder model for the siRNA moiety. The fitting of the experimental curves of siRNA led to a cylindrical shape whose volume was given by the following formula: $V(siRNA) = \pi \times radius^2 \times height$. Fitting of the curves of siRNA-SQ NPs gave a spherical distribution. The nanoparticle volume corresponded to: $(4/3) \times \pi \times radius^3$. Consequently, the ratio between the volume of the siRNA-SQ nanoparticle and the volume of the siRNA made it possible to determine the number of siRNAs linked to SQ in a nanoparticle.

### 2.12. Electrophoresis of siRNA PMP22-SQ NPs incubated in FBS or with serum components

Interactions between siRNA PMP22-SQ NPs and FBS or with one of its main components (BSA or LDL) were performed by incubating increasing amounts of FBS, BSA (molar ratio) or LDL (mass ratio) with 5 µM siRNA PMP22-SQ NPs for 30 min at 37°C. The same volume of each aliquot was loaded into 4% agarose electrophoresis gel stained with Midori Green Advance (Nippon Genetic Europe, Germany) that only reveals the oligonucleotides. The molecular weight (MW) size marker served as an evidence to testify the migration of siRNA PMP22-SQ NPs. Bands were revealed by camera under UV lamp illumination and recorded by Visio-capt 14.2 software.

### 2.13. BSA Fluorescence quenching

A series of BSA solutions at a fixed concentration (5 µM) incubated with an increasing amount of siRNA PMP22-SQ NPs (BSA/siRNA PMP22-SQ molar ratios = 0.5, 1, 2, 4 and 8 ) were analyzed. Solutions were filled into Hellma quartz Ultra-Micro cells and placed in a Cary Eclipse fluorimeter (Varian, Oxford, UK) for measurements. The samples were excited at 280 nm and emission scans were recorded between 300 and 550 nm. Spectra were averaged over 5 measurements. Quenching experiments could affected by the inner filter effect, where the sample could attenuate both the excitation beam and the emission spectrum. However, in our case, we worked with rather low concentrations of both BSA and siRNA PMP22-SQ NPs, and the optical density of the solutions was below 0.1; thus, this effect could be ruled out.

### 2.14. Steady-state fluorescence

To a fixed concentration of siRNA PMP22-SQ NPs (5 µM, *i.e.* 0.065 mg/mL), the BSA (100 µM stock solution) or LDL (2.5 mg/mL stock solution) were gradually added to achieve a final molar ratio of 1 [siRNA PMP22-SQ]:1 [BSA 5 µM] or mass ratio of 1 [siRNA PMP22-SQ]:2 [LDL 0.12 mg/mL]. Briefly, 1 mL of a 5 µM or 0.065 mg/mL siRNA PMP22-SQ NPs solution was filled into a Hellma Ultra-Micro quartz cell and 2 µL of BSA or LDL were progressively added until reaching the final ratio. In parallel, BSA and LDL were added to water to reach the same final concentration. After each addition, samples were excited at 280

nm and the fluorescence emission spectra were recorded from 300 to 400 nm using a Horiba Jobin Yvon Fluorolog 3 spectrometer.

### 2.15. Synchrotron radiation circular dichroism (SRCD)

Synchrotron radiation circular dichroism (SRCD) experiments were performed on the DISCO beamline at the SOLEIL Synchrotron (Saint Aubin, France). The conformation of naked siRNA PMP22 at two stages of NPs preparation (before and after the nanoprecipitation) was performed, as well as, the study of the interaction with BSA by mixing siRNA PMP22-SQ NPs and BSA at a volume/volume ratio of 1 [siRNA PMP22-SQ]:1 [BSA]. Four µL droplets of the samples were placed in 3.7 µm path length $CaF_2$ cells (Hellma). The raw spectra were acquired with a 1 nm spectral resolution. The spectra presented in this study were treated with CDTool software that can be freely downloaded at http://www.cdtools.cryst.bbk.ac.uk/ (Miles and Wallace 2018). Each is the average of three spectra. A background (water or corresponding buffer spectrum recorded under the same conditions) was subtracted. Intensity calibration was obtained with a camphor sulfonic acid CSA scale standard sample. Intensities were converted from millidegrees (θ machine units) into Δε using the formula $\Delta\varepsilon = \theta\times(0.1\times MRW)/(3298\times l^{*}C)$, where MRW is the mean residue weight of the BSA (protein weight/number of residues = 114 Da), $l$ is the path length of the $CaF_2$ cell in cm and $C$ is the protein concentration in mg/ml. In some cases, we have added a smoothing function.

### 2.16. Statistical analysis

Statistics were computed with GraphPad Prism 8.3.0 software. When we had two groups to compare, the Mann-Whitney analysis was performed to assess the statistical difference. For studies requiring grouped analyses, a one-way ANOVA followed by Bonferroni multiple comparison test was performed. A value of $p<0.05$ was considered significant.

# 3. Results

## 3.1. Structure determination of siRNA-SQ NPs

### 3.1.1. The physico-chemical characteristics of squalenoyl siRNA nanoparticles are nucleoside sequence-independent

To obtain nanoparticles, an inverse nanoprecipitation method (Bilati, Allémann et al. 2005) was performed by the addition of the aqueous solution containing the siRNA-SQ bioconjugates into acetone as an organic solvent, where siRNA-SQs were not soluble. The size and polydispersity of two resulting nanoformulations with siRNA RET/PTC1 or siRNA PMP22 were measured by DLS (**Figures 1A and 1B**). For the siRNA RET/PTC1, conjugation to SQ led to 180 nm NPs with a homogeneous distribution as indicated by the polydispersity index (PDI; less than 0.2). Surface charge of NPs was negative, around -35 mV, which favors colloidal stability of the NP suspension (**Figure 1C**). For siRNA PMP22, the results were similar: NPs size was 218 nm, PDI < 0.2 and surface charge -40 mV. No significant difference was observed between siRNA RET/PTC1-SQ and siRNA PMP22-SQ NPs in terms of size, polydispersity index and ζ-potential (**Figures 1A, 1B and 1C**). As no significant difference was found concerning the physicochemical parameters of both siRNAs (PMP22 or RET/PTC1) and previously with the siRNA TMPRSS2-ERG (Massaad-Massade, Boutary et al. 2018), it was decided to continue further experiments with the siRNA PMP22-SQ NPs. This resolution is also supported by our recent findings showing that the siRNA PMP22-SQ NPs could lead to a targeted therapy for CMT1A neuropathy (Boutary, Caillaud et al. 2021).

Then, the siRNA PM22-SQ NPs were observed by cryo-TEM (**Figure 1D**). Spherical nano-objects of around 130 nm in size were observed. Interestingly, the shape and size were in accordance with our previous observations (Massaad-Massade, Boutary et al. 2018).

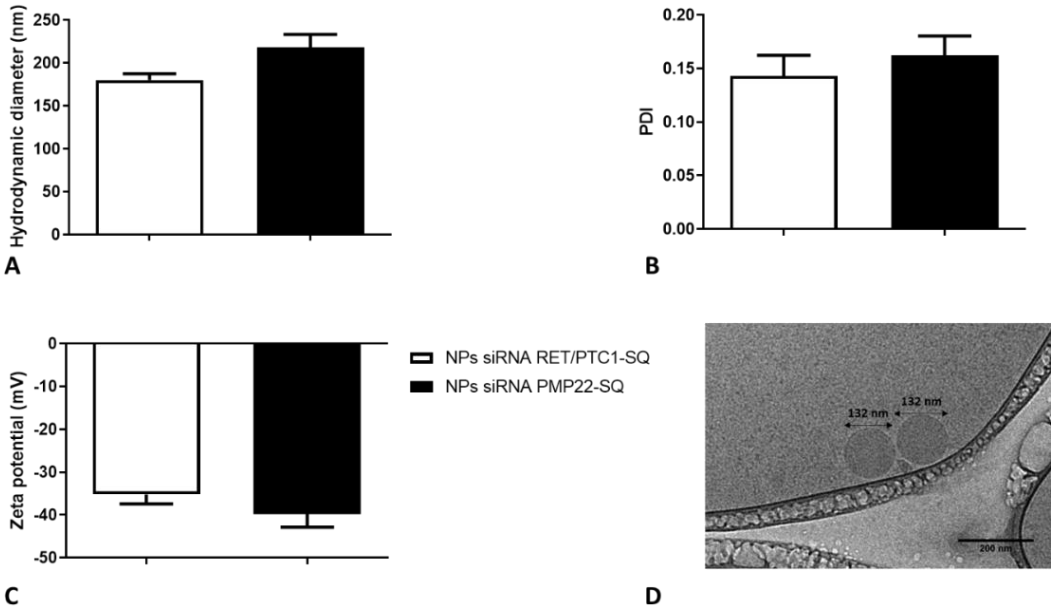


**Figure 1: Physicochemical characterization of siRNA-SQ NPs**. After inverse nanoprecipitation of siRNA RET/PTC1-SQ NPs and siRNA PMP22-SQ NPs the size (A) and polydispersity index (B) were measured by dynamic light scattering and the surface charge (C) by electrophoretic light scattering. Three measurements were performed and the average diameter ± standard error of the mean (SEM) of more than 5 independent nanoformulations, was calculated. Using the Mann and Whitney test, no significant difference between the two nanoformulations was found. D) Micrography of siRNA PMP22-SQ NPs by cryoTEM. The siRNA-SQ NPs are spherical with a diameter of around 130 nm.

#### 3.1.2. Inversion from negative to positive charge of siRNA-SQ NPs improves their transfection

To understand the impact of surface charge on the internalization of siRNA-SQ NPs, several experiments were conducted *in vitro*. Previously, we showed that the siRNA-SQ NPs were unable to enter cultured cells spontaneously without any cationic transfection agent (Raouane, Desmaele et al. 2011, Ali, Maksimenko et al. 2014, Boutary, Caillaud et al. 2021). We postulated that the negative surface charge of siRNA-SQ NPs prevented cell uptake due to electrostatic repulsion with the negative plasma membrane. It is well known that cationic nanoparticles had a higher internalization rate than neutral and negative nanoparticles. This difference can be explained by Coulomb's law, where opposite charges are attracted to each other. Thus, the cationic nanoparticles can be delivered to the cytoplasm by electrostatic attraction with the negatively charged cell membranes. To confirm this assumption, we modified the nanoparticle charge by addition of cationic guanidium-squalene to the siRNA-SQ NPs (**Figure 2A**). The resulting positive nanoparticles were then incubated with BHP 10-3 and MSC80, two cell lines of different origins (tumoral and normal). Interestingly, the

inhibition of the targeted gene expression without using lipofectamine testified that the uptake of the nanoparticle is facilitated by the use of a cationic compound (**Figures 2B and 2C**).

| | Size | PDI | Zeta potential |
|---|---|---|---|
| siRNA-SQ NPs | 171.3 ± 12.3 nm | 0.127 ± 0.019 | -37.1 ± 2.4 mV |
| siRNA-SQ NPs : $SQ^+$ | 225.5 ± 8.5 nm | 0.119 ± 0.014 | 39.6 ± 4.3 mV ** |

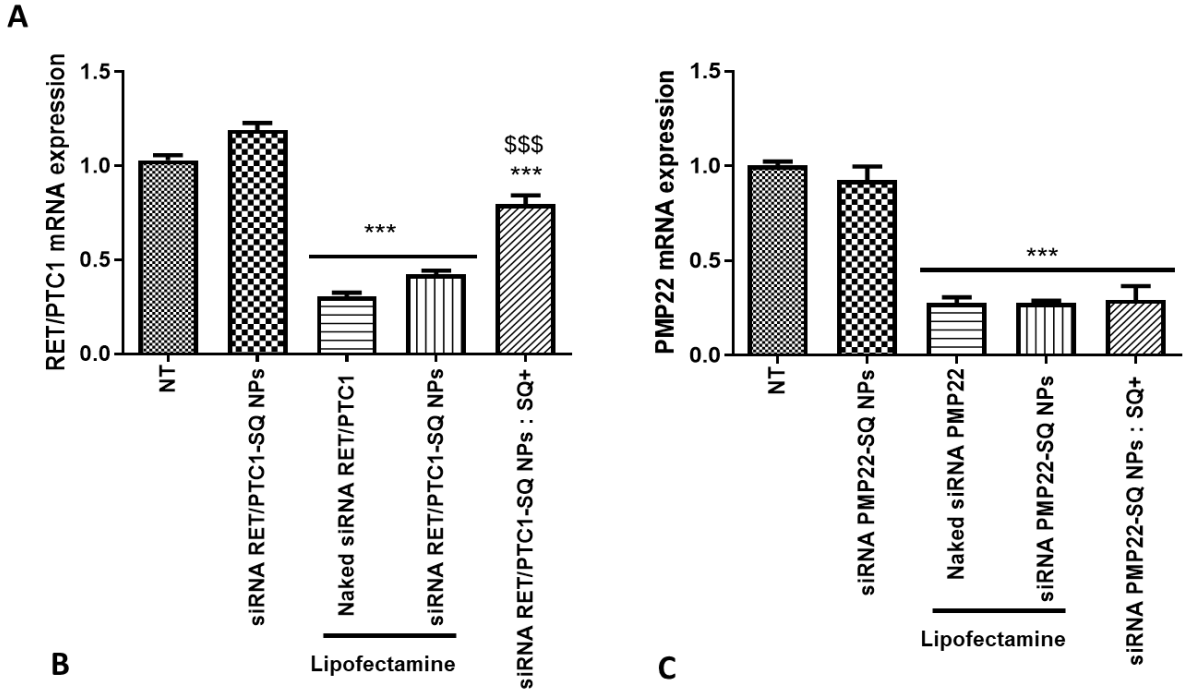


**Figure 2: Positively charged siRNA-SQ NPs are successfully cell internalized**. **A)** Physicochemical characteristics of NPs. No statistical difference was observed between siRNA-SQ NPs and siRNA-SQ NPs: $SQ^+$ for their size and PDI. Using the Mann-Whitney test, a statistical difference was found concerning the zeta potential between the siRNA-SQ NPs and siRNA-SQ NPs:SQ+ ($p < 0.001$). **B and C)** mRNA inhibition. BHP 10-3 **B)** and MSC80 **C)** cells were transfected with 50 nM siRNA RET/PTC1 or PMP22-SQ NPs with or without $SQ^+$. NT: non-treated cells. Lipofectamine was also used to transfect the naked siRNA and siRNA RET/PTC1 or PMP22-SQ NPs (positive controls). 48 hours later, cells were harvested, RNA was extracted, and RT-qPCR performed. One-way Anova followed by a Bonferroni test was used to assess the significant difference between treatments: *** $p < 0.0001$, compared to NT and untransfected targeted gene-SQ NPs ; $$$ $p < 0.0001$ when compared to transfected naked siRNA RET/PTC1 and siRNA RET/PTC1-SQ NPs by lipofectamine.

### 3.1.3 Spherical nanoparticles contain core/shell assemblies

Based on our previous results showing impressive therapeutic results in several tumor models (thyroid and prostate cancers (Ali, Urbinati et al. 2012, Urbinati, Hafiz et al. 2013, Ali, Maksimenko et al. 2014, Ali, Urbinati et al. 2014, Urbinati, Ali et al. 2015, Urbinati, de Waziers et al. 2016) as well as in monogenic neuropathy (CMT1A (Boutary, Caillaud et al. 2021)) and considering that cationic lipid have a higher *in vivo* toxicity (Caillaud, El Madani et al. 2020), we decided to deeply characterize the conjugated siRNA-SQ nanoparticles.

To verify that the conjugation to SQ and the formulation as nanoparticle did not induce changes in siRNA conformation, circular dichroism measurements were performed. As shown in **Figure S2A,** naked siRNA PMP22 and siRNA PMP22-SQ both before and after nanoprecipitation displayed the same spectrum type, confirming that the α–helix structure of the siRNA was kept intact after chemical conjugation to SQ and formulation as nanoparticles. Small-angle scattering methods are prominent tools for characterizing such nanometric colloidal suspensions. Taking advantage of the high difference of the scattering length density between hydrogen and deuterium, small-angle neutron scattering (SANS) represents, indeed, a method of choice to characterize the size distribution of hydrogenated colloids in a deuterated solvent and it has been proven previously to be a good way of characterizing the size of the squalene-based nanoparticles (Saha, Testard et al. 2015, Rouquette, Ser-Le Roux et al. 2019, Gobeaux, Bizeau et al. 2020). On the other hand, small-angle X-ray scattering (SAXS), which is sensitive to contrasts in electron densities, offered a description of the squalenoyl siRNA nanoparticles with deeper access to their internal structure. In the case of siRNA PMP22-SQ NPs, it was relevant to combine SANS and SAXS analysis since the former would be capable of detecting a larger contrast between the solvent and the full squalene derivative, and the latter between the solvent and the siRNA moiety (**Figure 3A**). The SANS of a 45 µM suspension of siRNA PMP22-SQ NPs is shown in **Figure 3B**. This pattern was not sensitive to dilution and the nanoparticle size remained stable under a dilution factor of two (**Figure S2B)**. The absence of structural peaks in the wide-angle region ($q$ > 0.04 $Å^{-1}$) indicated that the nanoparticle core displayed no regular crystal-like structure, in accordance with cryo-TEM images (see **Figure 1**). In the medium $q$-range (0.006 to 0.02 $Å^{-1}$), the scattering intensity followed a power-law in $q^{-3.44}$ slightly deviating from the $q^{-4}$ expected for sharp interfaces (Porod's Law (Guinier, Fournet et al. 1955)) between particle surfaces and solvent. If such observation may eventually indicate a slightly diffuse or fractal interface, it was however unlikely, given that the siRNA PMP22-SQ NPs surface appeared rather smooth in the cryo-TEM images. At the lowest wavevectors, the scattering intensity reached the onset of a plateau indicating a finite size. A simple Guinier analysis gave a gyration radius ($R_g$) of 80 nm that corresponded to a hydrodynamic radius (as it would be determined by DLS) of 103 nm for a spherical shape. Overall, this scattering pattern could be fitted by considering a lognormal distribution of spheres (black line on red pattern in **Figure 3B**), with a median radius of 61.9 nm and a polydispersity index (PDI) of 0.25. The corresponding diameter distribution resulting from this fit is presented in **Figure 3C**.

The SAXS pattern of a 263 µM solution of siRNA PMP22-SQ NPs (blue pattern) is presented in **Figure 3D**. Again, no specific structural peak could be observed in the large *q* region ($q > 0.3$ Å$^{-1}$). On the contrary to the SANS pattern, two large oscillations were visible in the middle *q*-range ($0.007 < q < 0.3$ Å$^{-1}$), that could be attributed to siRNA moieties in the nanoparticle or at least to electronic density heterogeneities in the particle. As a matter of comparison, the SAXS pattern of the siRNA PMP22 moiety (224 µM) was also plotted (green pattern). The scattering pattern originating from the naked siRNA PMP22 dispersion exhibited an oscillation in the same *q*-range and could be fitted by a cylindrical form factor ($L$ = 7.1 nm, $R$ = 1.1 nm), in accordance with the SANS analysis of similar siRNA strands reported by Ristori *et al.* (Ristori, Ciani et al. 2012) (**Table S1**).This characteristic shape was found again in the oscillation, visible in the large *q* of the siRNA PMP22-SQ pattern, yielding the following dimensions: $L$ = 4 nm and $R$ = 1.1 from the fitting by a cylindrical form factor. The other oscillation (at lower *q*) could be fitted by spheres with a radius of 5.5 nm. Since these spheres could accommodate the siRNA strands, we suggested that the siRNA PMP22 moieties were segregated and surrounded by the squalene moiety in core/shell assemblies with interconnections of the squalene moieties within the NPs. The obtained dimensions indicated a heterogeneity in electronic density inside the NPs, but without long range ordering.

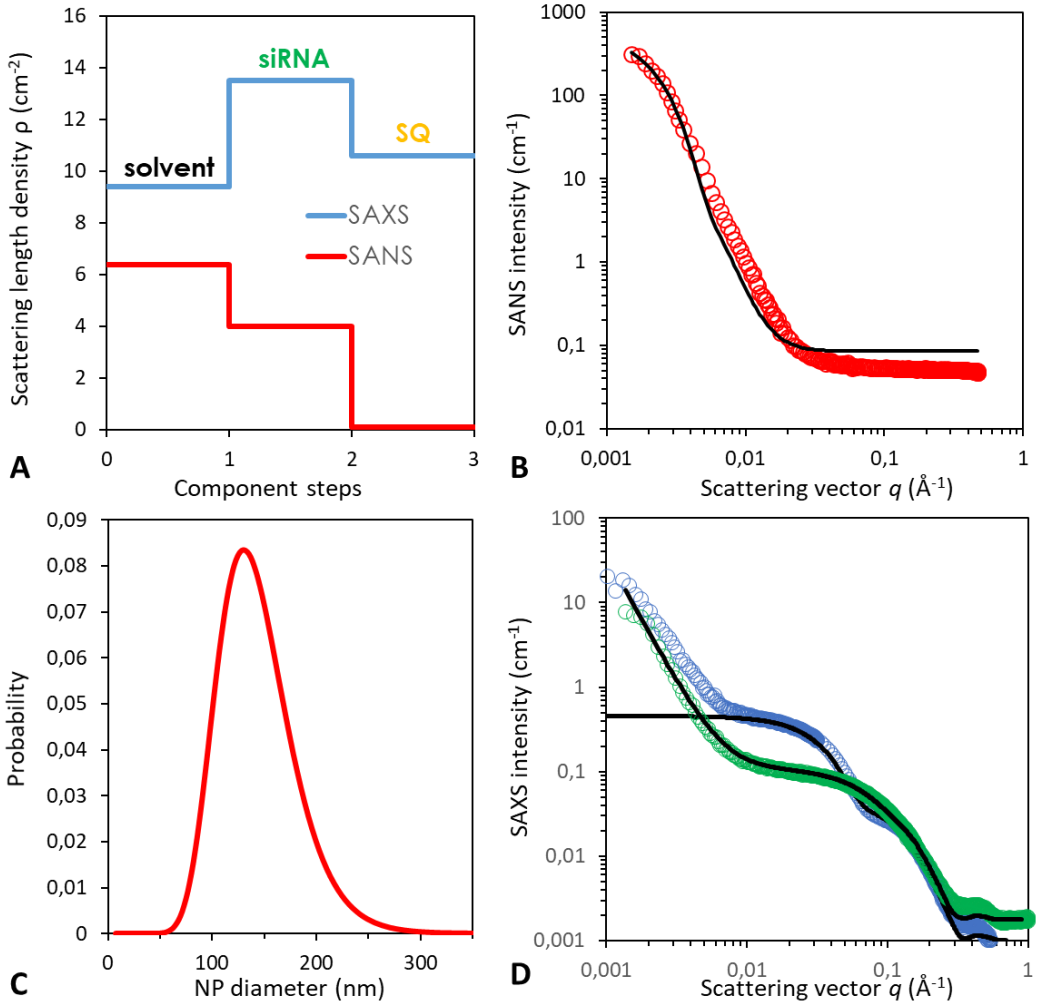


**Figure 3: Structural characterization of siRNA PMP22-SQ NPs by small-angle scattering.**

**A)** Scattering length densities show that the SANS approach allows to characterize the overall structure of the nanoparticles and the SAXS analysis to characterize the siRNA encapsulated within the NPs. The solvent used are $H_2O$ and $D_2O$ for SAXS and SANS, respectively. **B)** SANS pattern for siRNA PMP22-SQ NPs (open circles) depicting a fit with a lognormal distribution of spheres (black trace). **C)** SANS view software analysis of the fit B showed that the corresponding siRNA PMP22-SQ NPs diameters are 124 nm. **D)** SAXS patterns of the naked siRNA PMP22 (green circles) and of siRNA PMP22-SQ NPs (blue circles) with their corresponding fits (black traces). The naked siRNA PMP22 can be fitted by a 7 nm-long cylindrical shape and a scattering in $q^{-3}$ in the low $q$ range (a signature of aggregation). A combination of 4 nm cylindrical and 11 nm spherical shapes was found for the internal organization of the siRNA PMP22-SQ NPs.

### 3.1.4. A 130 nm nanoparticle can encapsulate around 60 000 siRNAs

The structural model of siRNA PMP22-SQ NPs is illustrated by the sketch in **Figure 4**. The siRNA PMP22-SQ bioconjugate monomer is represented by a green cylinder for the siRNA moiety and a yellow lipid tail for the squalene moiety (**Figure 4A**). The

supramolecular organization inside the nanoparticle is represented by 11-nm core/shell spheres with the lipidic moieties surrounding the hydrophilic siRNAs (**Figure 4A**). As no specific inner structure was apparent in the cryo-TEM images, the core/shell structures were supposed to be randomly distributed inside the whole nanoparticle volume. Therefore, representation of a top view nanoparticle cross-section depicts a random pattern of circular motifs (**Figure 4B**). Since the formation of squalene-based nanoparticles was clearly driven by hydrophobic interactions (Lepeltier, Bourgaux et al. 2014), we assumed that the squalene shells around the hydrophilic siRNA core could be interpenetrated and formed a continuous lipophilic network and it is most likely that some charged hydrophilic siRNA strands point towards the solvent (represented by the green circle around the yellow one in **Figure 4B**). By a simple geometrical calculation (volume of nanoparticle/volume of siRNA), we could estimate that one nanoparticle contained on average 60,000 siRNA PMP22-SQ bioconjugates.

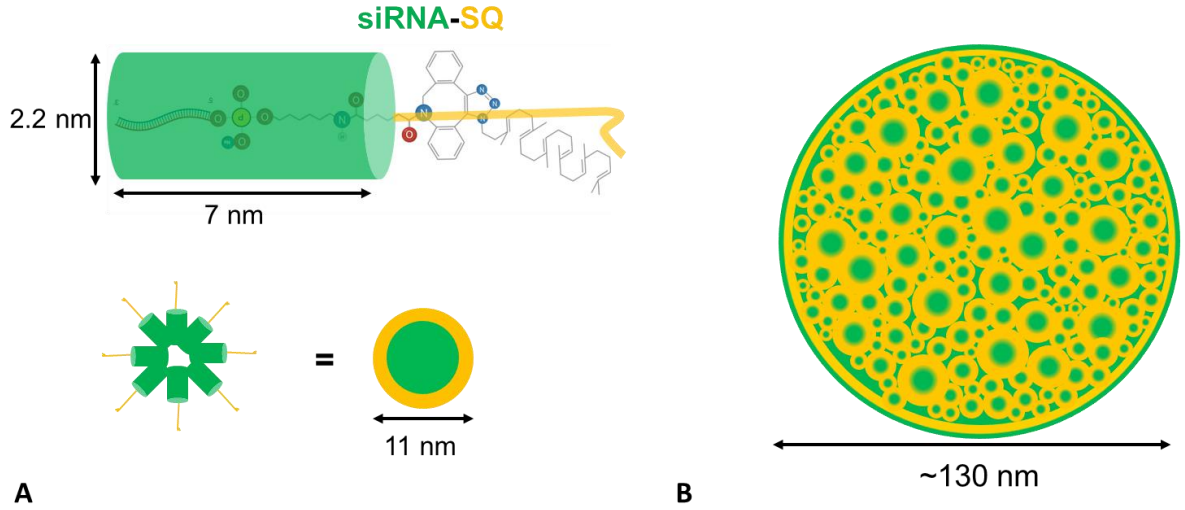


**Figure 4: Graphical representation of a siRNA PMP22-SQ nanoparticle as determined by the fit of the scattering patterns. A)** Sketch of siRNA PMP22-SQ monomer. The siRNA moiety (green) of the bioconjugate can be viewed as a cylinder (siRNA not to scale in comparison to others chemical entities). The squalene moiety is depicted in yellow. The SAXS pattern reveals 11-nm spherical structures inside the nanoparticle that we view as self-assembled core/shell domains with a siRNA core surrounded by squalene which could interpenetrate with the other squalene moieties. **B**) Representation of a cross-section of 2D siRNA PMP22-SQ nanoparticle. The core/shell spheres of 11-nm each are randomly arranged inside the nanoparticle. The 2D cross section is the cause of the difference in the core/shell sphere size in the sketch.

## 3.2. siRNA PMP22-SQ NP interactions with serum and its components

### 3.2.1. Serum components stabilize siRNA PMP22-SQ NPs

SANS was performed to determine the influence of fetal bovine serum (FBS), a biological medium with high ionic strength containing several proteins, on the structure of siRNA PMP22-SQ NPs. In the low *q* range ($q < 0.003$ Å$^{-1}$), the resulting SANS patterns did not show strong deviation from the scattering intensity of the siRNA PMP22-SQ suspension (at similar concentration) (**Figure 5A)**. No intensity increase was observed, as it could be expected when particles are growing or when attractive interactions appear between particles. It demonstrates that siRNA PMP22-SQ NPs were colloidally stable and did not aggregate in this complex mixture. On the contrary, the scattering intensity arising from the siRNA PMP22-SQ NPs slightly decreased. As confirmed by the fitting curve (black line on **Figure 5A**), the SANS pattern of the mixture appeared to be a linear combination of the two reference patterns. If we consider the formula: $I_{fit} = A \times I\text{single(siRNA PMP22-SQ NPs)}_{ini} + B \times I\text{single(FBS)}_{ini}$, the best fit was obtained for A = 0.87 and B = 0.98, demonstrating that only 13% of the siRNA PMP22-SQ signal had disappeared. The same result has been observed after incubation of siRNA PMP22-SQ NPs with a high concentration of bovine serum albumin (BSA) (200 µM, green pattern in **Figure 5B**). As with FBS, SANS patterns of BSA alone (red pattern) or siRNA PMP22-SQ NPs alone (blue pattern) were also recorded. Likewise, the scattering intensity was not much modified at small *q*. Thus, neither siRNA PMP22-SQ NPs nor FBS or BSA were significantly affected by the presence of each other. Therefore, it was concluded that siRNA PMP22-SQ NPs had a high colloidal stability in both biological media.

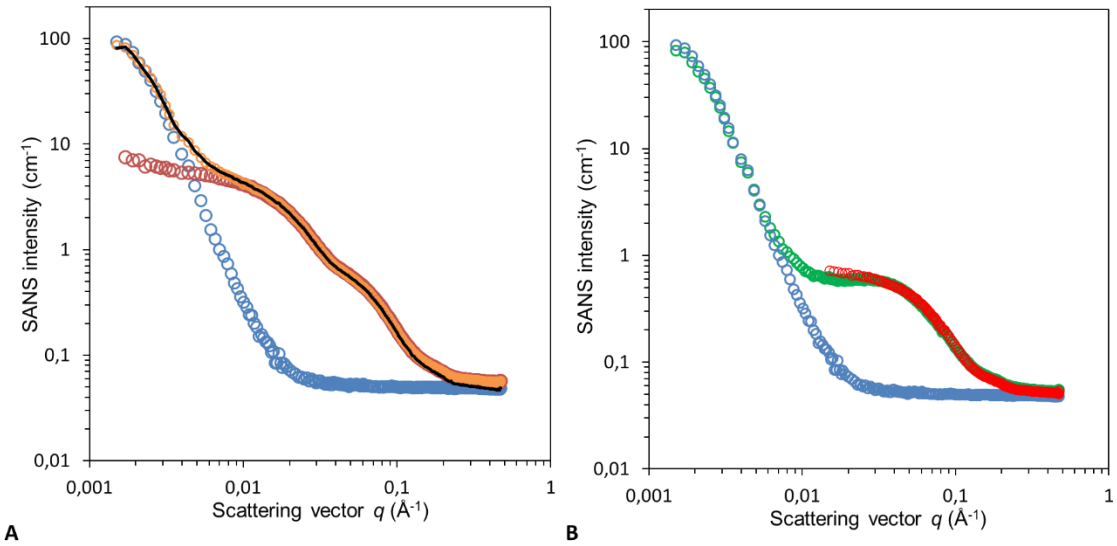

**Figure 5: The siRNA PMP22-SQ NPs are stable in FBS and in the presence of high BSA concentration**. **A**) SANS pattern of siRNA PMP22-SQ NPs/FBS mixture (yellow circles). Blue circles: 23 µM [siRNA PMP22-SQ] in $D_2O$, red circles: FBS dialyzed against $D_2O$ and diluted by a factor of 2 to reach the same concentration as in siRNA PMP22-SQ NPs/FBS mixture. The smooth black curve corresponds to a linear combination of the FBS and siRNA PMP22-SQ NPs curves. **B**) SANS pattern of siRNA PMP22-SQ NPs/BSA mixture (green circles). Blue circles: 23 µM [siRNA PMP22-SQ] in $D_2O$, red circles: 200 µM [BSA] in $D_2O$.

### 3.2.2. Serum neutralizes the siRNA-SQ NPs surface charge

The ζ-potential increased progressively towards neutrality when siRNA PMP22-SQ NPs were incubated with 0.2 % to 100 % of FBS (**Figure 6A**). The 100% of FBS represent its ζ-potential and is used as a control to discriminate the ζ-potential of the nanoparticles from the undiluted FBS. These results highlighted the strong interaction occurring between some FBS components and siRNA PMP22-SQ NPs. Interaction with serum components was also confirmed by electrophoresis (**Figure 6B**). A progressive slowdown of migration reflected by a delay in their electrophoretic mobility was observed when siRNA PMP22-SQ NPs were incubated in FBS (respectively around 350 kb for NPs with FBS as against around 150 kb for NPs in $H_2O$). Interestingly, this phenomenon was observed at very low FBS concentration (2%). Taken together, these results showed that FBS modified the surface charge and electrophoretic mobility of siRNA-SQ NPs.

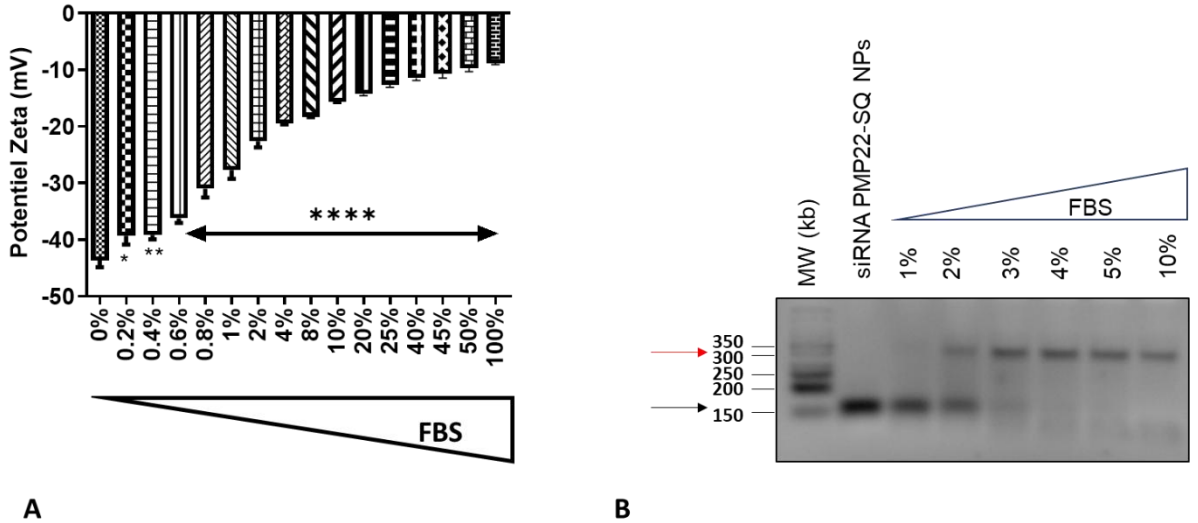


**Figure 6: siRNA PMP22-SQ NPs interact with serum components. A)** Measurements of the siRNA-PMP22-SQ NPs ζ-potential in the presence of increasing concentrations of FBS (from pure water (0% FBS) to pure FBS (100%). * $p < 0.05$, **$p<0.001$ and ****$p<0.00001$ by using One-way Anova followed by a Bonferroni test. **B**) The siRNA PMP22-SQ NPs were incubated with increased concentration of FBS and loaded onto 4% agarose electrophoresis gel, then stained by Midori, a nucleotide maker. Migration slows down when FBS is added to

586 the siRNA PMP22-SQ NPs (red arrow, wells 3 to 8), compared to siRNA PMP22-SQ NPs in
587 water (black arrow, well 1).

588 3.2.3. siRNA PMP22-SQ NPs interact with BSA

589 Albumin is the main serum component, representing around 55% of total protein
590 content. BSA has intrinsic fluorescence, due to its amino acid, tryptophan, which can be
591 recorded by fluorescence emission spectroscopy. Thus, the interaction between BSA and
592 siRNA PMP22-SQ NPs was investigated by two fluorescence spectroscopic approach: Stern-
593 Volmer quenching and steady-state fluorescence. First, by using the Stern-Volmer quenching
594 experiment, we showed an interaction between siRNA PMP22-SQ NPs and BSA (**Figure**
595 **7A**). Indeed, when BSA was incubated with increasing siRNA PMP22-SQ concentrations, the
596 intrinsic fluorescence of BSA was quenched, represented by a reduction of fluorescence
597 emission compared to BSA alone at 5 µM (red curve in **Figure 7A**). These results were
598 determined according to the Stern-Volmer equation described in **Supplementary**
599 **information, equation A**. The value obtained for the quenching rate constant, $K_{q,}$ was higher
600 than $10^{10}$ $mol.L^{-1}.s^{-1}$, suggesting a static mechanism with the formation of a complex between
601 BSA and siRNA PMP22-SQ NPs (**Table 1**). The equivalent of the affinity constant for the
602 kinetic intermediate, the Stern-Volmer constant, was equal to $2.60 \pm 0.80 \times 10^5$ $L.mol^{-1}$. All
603 the obtained values are presented in **Table 1**.

604 **Table 1: Numerical values based on linear fit of Stern-Volmer and Steady-state**
605 **equations**

| Constants | | Value | Unit |
|---|---|---|---|
| Quenching rate constant | $K_q$ | 2.60 ± 0.80 | $\times 10^{13}$ $L.mol^{-1}.s^{-1}$ |
| Stern-Volmer constant (kinetic intermediate) | $K_{sv}$ | 2.60 ± 0.80 | $\times 10^5$ $M^{-1}$ |
| Overall affinity constant (final thermodynamic complex) | $K_a$ | 2.34 ± 0.59 | x $10^7$ $M^{-1}$ |

606 In the steady-state fluorescence approach, BSA was progressively titrated against
607 siRNA PMP22-SQ NPs suspension, to a final molar ratio of 1 [siRNA PMP22-SQ]:1 [BSA].
608 In parallel, BSA was added to distilled water at the same concentration and the final spectra
609 were compared. The presence of siRNA PMP22-SQ NPs led to a significant modification of
610 the BSA emission spectrum (red curve in **Figure 7B**) compared to that of BSA alone in water
611 (black curve in **Figure 7B**). Indeed, we observed a smaller fluorescence intensity under the
612 final experimental conditions and a shift in the maximum fluorescence intensity (from 351 nm

for BSA alone to 349 nm for NPs-BSA), which indicated the formation of a complex between the two species (*i.e.*, siRNA PMP22-SQ NPs and BSA). The interaction mechanism could be probed by several equations according to the species in solution that are dependent on pH and temperature **(Supplementary information, equation B).** The linear least-squares regression showed good correlation between siRNA PMP22-SQ NPs and BSA (**Figure 7C**). The calculated overall apparent dissociation constant, $K_{obs}$, was equal to 4.95 ± 1.38 x $10^{-8}$ M (n = 3; pH 7) with an overall affinity constant, $K_a$, of 2.34 ± 0.59 x $10^7$ $M^{-1}$.

Using both spectroscopic approaches, we showed the formation of a complex between siRNA PMP22-SQ NPs and BSA. However, there was a disparity between the affinity constants obtained. This could be explained by the experimental conditions, especially the time (**Figure 7D**). Indeed, with Stern-Volmer quenching, a kinetic intermediate (BSA-NPs)′ was obtained with $K_a$' of 2.6 x $10^5$ $M^{-1}$. The slow titration of the steady-state fluorescence led to the final thermodynamic complex between BSA and NPs: BSA-NPs ($K_a$ = 2.34 ± 0.59 x $10^7$ $M^{-1}$). Therefore, the intermediate complex underwent a conformational change which allowed to attempt its final thermodynamic state by increasing even more the stability of the complex by a factor of 100.

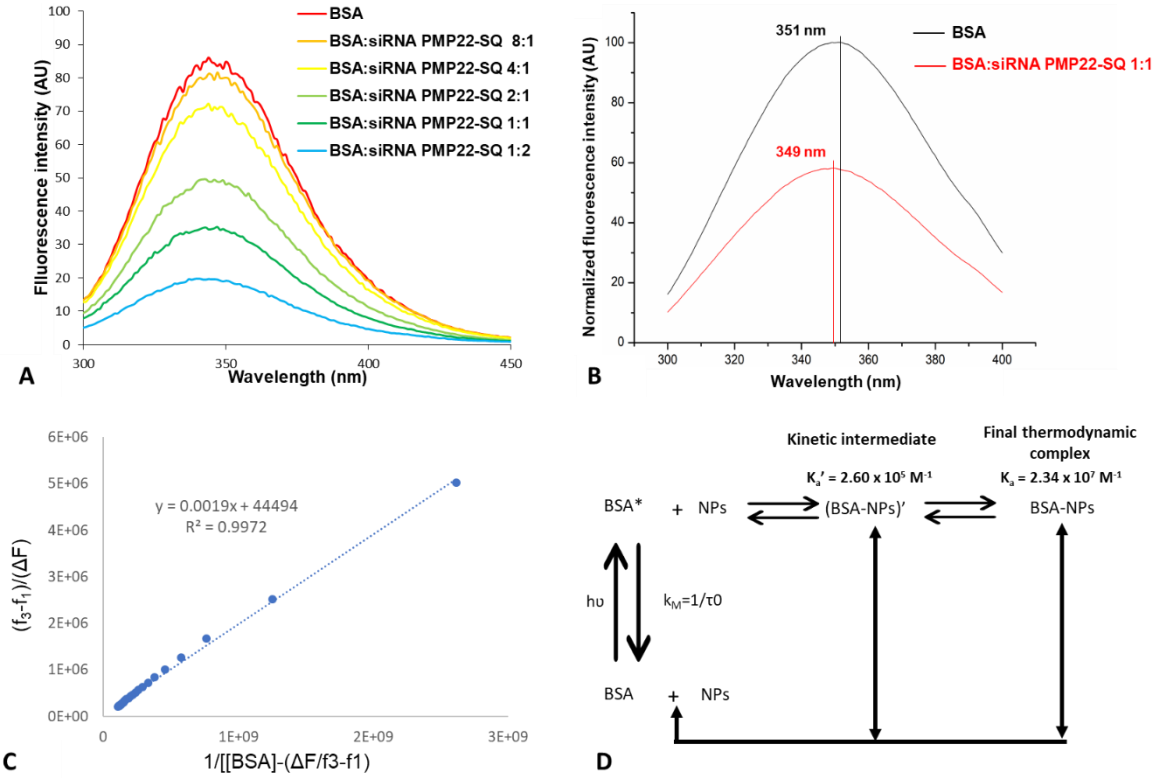


**Figure 7: Spectroscopic analysis of siRNA PMP22-SQ NPs/BSA mixtures**. **A)** Stern-Volmer quenching of BSA in the presence of siRNA PMP22-SQ NPs. The fluorescence intensity of BSA decreases progressively in the presence of siRNA PMP22-SQ NPs. **B)** Steady-state experiment showing the emission fluorescence spectra at the end of the

experiment, excitation wavelength ($\lambda_{ex}$ = 280 nm), pH 7.4 at 37°C: BSA (5 µM, black curve) and BSA (5 µM) + siRNA PMP22-SQ (5 µM) in red. The maximal fluorescence intensity decreases, and the emission wavelength shifts by 2 nm (from 351 nm to 349 nm) when BSA interacts with siRNA PMP22-SQ NPs. Fluorescence intensity has been normalized on BSA maximum peak. **C)** Linear least-squares regression of the formula given in the **Supplementary information, equation 2** ($R^2$ = 0.9972)**. D)** Graphical representation showing the relationship between Stern-Volmer and steady-state approaches, showing the affinity constants, $K_a$' and $K_a$

The interaction between BSA and siRNA PMP22-SQ NPs was further investigated by circular dichroism spectroscopy (**Figure 8A**). Incubation of BSA with siRNA PMP22-SQ NPs resulted in a decrease of 8% to 10% in the absolute signal intensity. Secondary structure quantifications of BSA was performed by using BestSel software, showing a slight decrease in the number of α-helices, similarly to concentrated BSA (**Figure S3**). This interaction between BSA and siRNA PMP22-SQ NPs was also tested by electrophoresis gel. Migration of siRNA PMP22-SQ NPs was slowed down after incubation with increasing concentrations of BSA (**Figure 8B**). At molar ratio [siRNA PMP22-SQ] 1: 4 [BSA], migration delay was maximum and we estimated that around 10 BSA molecules surrounded 1 nanoparticle (**Supplementary information, equation C).** Taken together, both results highlighted the formation of a NPs-BSA complex. However, this complex was not able to modify the BSA secondary structure.

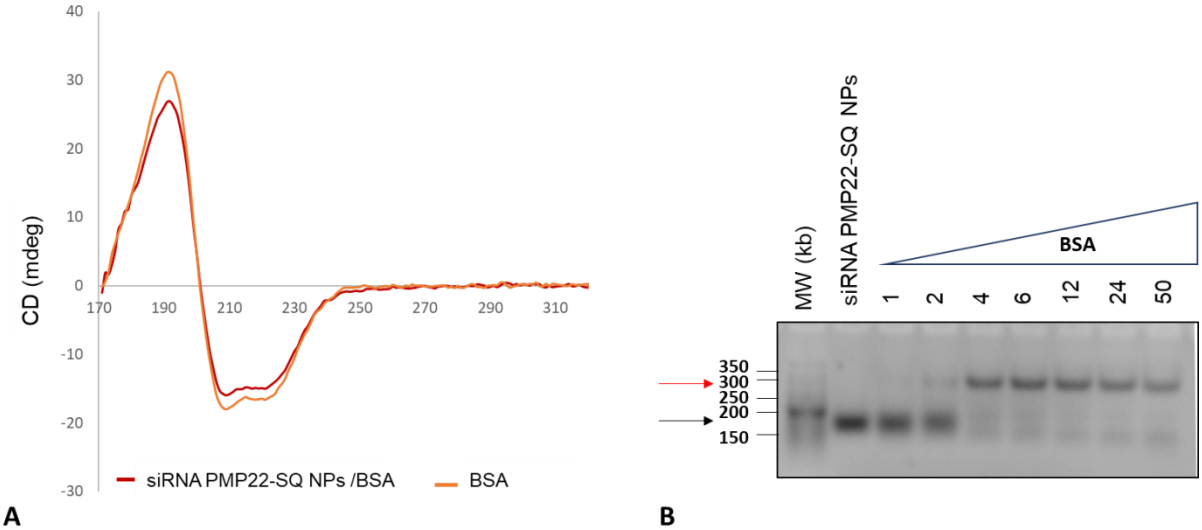


**Figure 8: siRNA PMP22-SQ NPs interact with BSA**. **A)** Circular dichroism spectrum of BSA alone (orange curve) and in the presence of siRNA PMP22-SQ NPs (red curve). In water, BSA spectra exhibits one positive peak at 192 nm and two negative bands at 210 and 224 nm, both characteristic of the α-helical structure. A decrease in the BSA signal in the presence of siRNA PMP22-SQ NPs is observed. **B)** Gel electrophoresis representing the migration of the siRNA PMP22-SQ NPs (5 µM) incubated at 37°C with increasing BSA

concentration loaded on 4% agarose gel. Migration progressively slows down (red arrow, wells 4 to 8), compared to siRNA PMP22-SQ NPs in water (black arrow, well 1).

### 3.2.4. siRNA-SQ NPs interact with LDL.

Finally, we focused on the low-density lipoproteins (LDL), that carry 75% of blood cholesterol in humans. Incubation of siRNA PMP22-SQ NPs with increasing amounts of LDL showed a slowdown of the gel electrophoresis migration testifying an interaction between the two species (**Figure 9A**). In addition, ζ-potential measurements revealed a significant progressive increase of the NPs surface charge with increasing LDL concentration (**Figure 9B**). These results were confirmed by the fluorescence spectrum of the LDL (**Figure 9C)**, which weakened in the presence of the NPs and was accompanied by a 5-nm shift in the peak emission wavelength. This clearly confirmed the formation of a siRNA PMP22-SQ NPs - LDL complex.

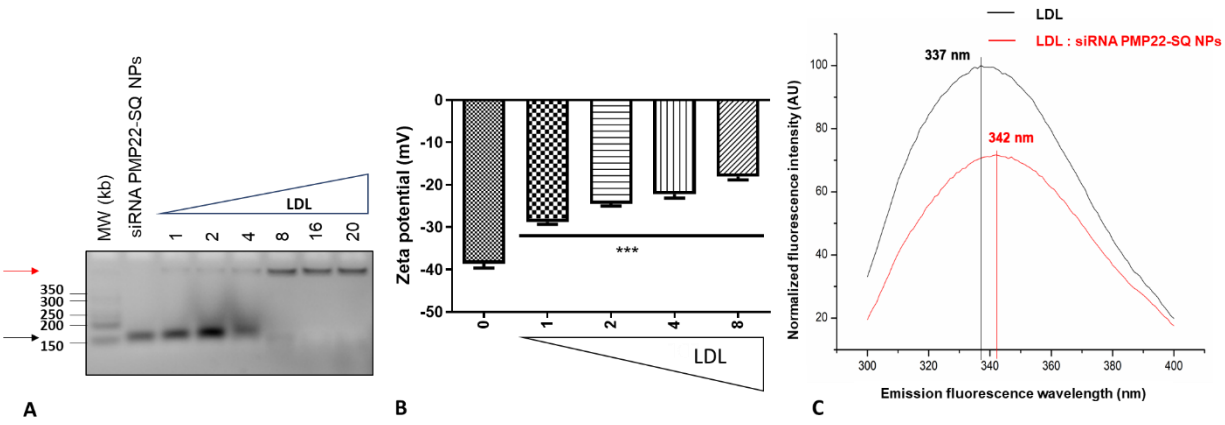


**Figure 9: siRNA-SQ NPs interact with LDLs**. **A)** Gel electrophoresis showing the migration of siRNA PMP22-SQ NPs incubated at 37°C with increasing LDL concentration loaded on 4% agarose gel. Migration progressively slows down (red arrow, wells 5 to 7), compared to siRNA PMP22-SQ NPs in water (black arrow, well 1). **B)** ζ-potential measurement after incubation with growing concentrations of LDL. *** $p < 0.0001$ *vs* siRNA PMP22-SQ NPs (One-way Anova followed by a Bonferroni test). **C)** Emitted fluorescence spectrum of LDL in the absence (black curve) or presence of siRNA-SQ NPs (red curve). The maximal fluorescence intensity decreases and there is a 5 nm shift of emission peak (from 337 nm to 342 nm) when LDL interacts with siRNA PMP22-SQ NPs. Fluorescence intensity has been normalized to LDL peak maximum.

### 3.2.5. siRNA PMP22-SQ NPs interact via the squalene moiety with serum components

NPs made from small molecules linked to squalene, including nucleoside analogs, interact with serum components *via* the SQ moiety (Sobot, Mura et al. 2017, Sobot, Mura et al. 2017, Yesylevskyy, Ramseyer et al. 2018). To confirm that similar interaction could occur

with siRNA PMP22-SQ NPs and FBS or its components (*i.e.*, BSA and LDL), naked siRNA PMP22 (*i.e.* not conjugated with SQ) was incubated with increasing amounts of whole serum, BSA or LDL, before electrophoresis were performed. Contrary to siRNA PMP22-SQ NPs, migration of serum and serum components did not slow down (**Figure 10**). This confirmed that the interaction of nanoparticles with serum components occurred well *via* the squalene moiety and not *via* the oligonucleotide moiety.

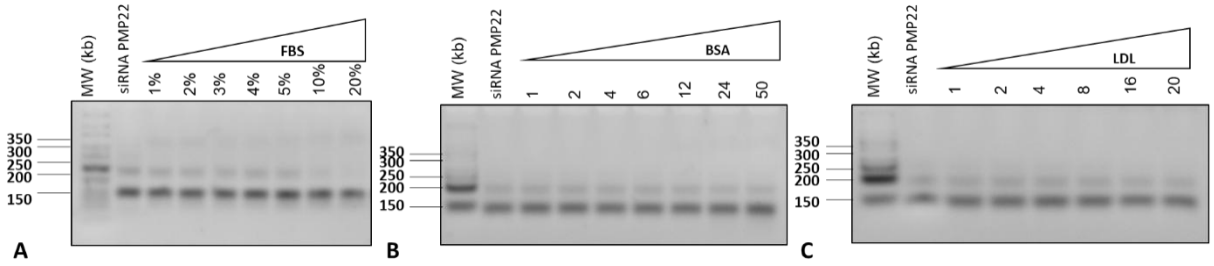


**Figure 10: Naked siRNA PMP22 do not interact with total serum, BSA and LDL**. 4% non-denaturated agarose electrophoresis were performed after incubation of naked siRNA PMP22 with increasing amounts of FBS **(A)**, BSA **(B**, molar ratio**)** and LDL **(C**, mass ratio**)**. No slowdown of migration was observed.

## 4. Discussion

Conjugation of siRNA to squalene by Cu-free click chemistry, has been previously demonstrated to protect the double-strand oligonucleotide from degradation and to treat different experimental diseases such as cancer with fusion oncogene or peripheral neuropathy (Massaad-Massade, Boutary et al. 2018, Boutary, Caillaud et al. 2021). To be injectable and efficient *in vivo*, squalenoyl siRNAs needed to be formulated as nanoparticles. However, due to the different molecular weight of the two bioconjugate moieties (*i.e.*, ~ 13,000 Da for siRNA /~ 494 Da for SQ forming a ratio of 26/1 between hydrophilic siRNA and lipophilic squalene) and because the siRNA-SQ bioconjugates were not soluble in organic solvents but totally soluble in water, an inverse nanoprecipitation protocol has been optimized by adding the aqueous phase to the organic one, before solvent evaporation to obtain the final siRNA-SQ NPs suspension (Bilati, Allémann et al. 2005).

The size and size distribution of the nanoparticles are important parameters for drug delivery systems. Using DLS, a rapid method for determination of nanoparticles size, we found that the diameter of squalenoyl siRNA nanoparticles were nucleoside sequence independent. Indeed, both siRNA PMP22-SQ and RET/PTC1-SQ nanoparticles displayed similar dimension, around 200 nm with a negative charge less than -30 mV; they were stable for a month at 4 °C (Massaad-Massade, Boutary et al. 2018, Boutary, Caillaud et al. 2021). As no significant difference was found concerning their physicochemical parameters, it was

decided to use the siRNA PMP22-SQ NPs for all further experiments. This resolution was also supported by our recent findings concerning the therapeutic efficiency of siRNA PMP22-SQ NPs as a targeted therapy for CMT1A neuropathy (Boutary, Caillaud et al. 2021).

Then, the siRNA PM22-SQ NPs were observed by cryo-TEM. Spherical nanoobjects of around 130 nm in size with no specific internal structure were observed similar to our previous observation on siRNA TMPRSS2-ERG-SQ NPs, which confirmed once again that the size was independent of the nucleoside sequence (Massaad-Massade, Boutary et al. 2018). Of note, cryoTEM is more specific than DLS, since it provides additional information on shape and morphology. The smaller nanoparticles size observed by cryoTEM was explained by the fact that laser light scattering measured the hydrodynamic size when cryoTEM allowed to visualize the nanoparticle core only. Small-angle neutron scattering (SANS) confirmed the observed size and shape of the siRNA PMP22-SQ nanoparticles. Altogether DLS, cryo-TEM and SANS analysis represented complementary approaches, giving an ensemble picture of the siRNA PMP22-SQ NPs.

To describe more precisely the internal composition and the siRNA organization inside of the NPs, SAXS analysis have been performed, which depicted that the siRNA PMP22-SQ bioconjugates self-organized in water into small core/shell domains of 11-nm size with the lipidic moiety exposed to the outside and the siRNA located in the core, without modification of the α-helix structure of the nucleic acid. We assume that hydrophobic interactions are the main driving force leading to the self-assembly of the nanoparticle into a 130-nm size spherical random structure with some hydrophilic siRNA moieties being exposed onto the nanoparticle surface for solubility reasons. To our knowledge, this unique random supramolecular structure, composed of typical 11-nm size spheres with internal electronic density heterogeneities, has only been observed with siRNA PMP22-SQ NPs. It confirms the diversity of the squalenoyl nanostructures and the flexibility of the hydrophobic squalene chain which allows to self-assemble into nanoparticles, even when a hydrophilic macromolecule of much higher molecular weight was attached to the SQ.

We then assessed the interaction of siRNA PMP22-SQ NPs with blood components, specifically albumin and lipoproteins. Indeed, once administered intravenously, siRNA-SQ NPs encounter different blood components that can adsorb to the NPs surface, either stabilizing or destabilizing their structure and this may dramatically impact their *in vivo* fate in terms of biodistribution, pharmacokinetics, toxicity and therapeutic efficiency (Aggarwal, Hall et al. 2009, Lesniak, Fenaroli et al. 2012, Monopoli, Aberg et al. 2012, Gao and He 2014, Marichal, Giraudon-Colas et al. 2019, Marichal, Degrouard et al. 2020).

It was observed that siRNA PMP22-SQ nanoparticles interacted hydrophobically, *via* the squalene moiety, with serum components, especially BSA and LDL. Interestingly, it has been reported that BSA may display some dysopsonin-like activity (Ogawara, Furumoto et al. 2004). These interactions with serum components can undergo conformational changes on the NPs surface which could also affect their biological fates (Gunawan, Lim et al. 2014). This hypothesis was assessed by SANS experiments performed in FBS and in presence of high BSA concentrations. No significant modifications in the SANS pattern of the nanoparticles could be observed. This proved that the siRNA PMP22-SQ NPs kept high colloidal stability in biological media, contrarily to previous studies performed with small chemical molecules conjugated to squalene showing a destabilization of the squalenoyl NPs in the presence of blood components, with an insertion of these bioconjugates, as molecular entities, into the LDL and BSA fractions (Ambike, Rosilio et al. 2011, Sobot, Mura et al. 2017, Yesylevskyy, Ramseyer et al. 2018, Gobeaux, Bizeau et al. 2020). Thus, the present study clearly suggests that the biological behavior of squalene-based nanoparticles may depend on the nature of the associated biologically active molecule. Such different behavior of squalenoyl NPs may be explained by: i) the respective molecular weight of the linked drug *versus* the squalene (*i.e.*, a ratio of 1 or 2 *vs* 26 with siRNA-SQ), ii) the different physicochemical parameters (siRNA-SQ is highly negatively charged) and, iii) the supramolecular organization.

Since LDL and HDL are the main transporters of cholesterol, an important lipid for tumor cell proliferation (Chaudhary, Bower et al. 2019) and myelin synthesis (Zhou, Bazick et al. 2019) , we hypothesize that the interaction of LDL with siRNA PMP22-SQ NPs may trigger a natural nanoparticles functionalization for targeting these pathological tissues. Additionally, such specific biodistribution may be amplified by the inflammation of the pathological tissues, resulting in histological modifications such as defective endothelial cells with wide fenestrations in cancer tissues (Tatiparti, Sau et al. 2017, Hoogenboezem and Duvall 2018) and edema with lymphocyte infiltration in neurodegenerative diseases (Weis, Claeys et al. 2017). Especially, albumin accumulate preferentially in these type of tissues (Hoogenboezem and Duvall 2018). Thus, siRNA-SQ NPs are expected to extravasate through damaged tissues, as supported by our previous studies for cancers and a disease of the peripheral nervous system (CMT1A), where in both pathologies a significant inhibition of the targeted gene was observed in the tissues concerned (Massaad-Massade, Boutary et al. 2018, Boutary, Caillaud et al. 2021).

## 5. Conclusions

The present study has provided an important contribution to better understand the physico-chemical structures of siRNA squalene-based nanoparticles, as well as their interactions with some biological components encountered after intravenous administration. The high specificity of siRNA to decrease or normalize gene expression offers new outlooks to cure pathologies with gene expression dysregulation such as fusion oncogene cancer or hereditary monogenic peripheral neuropathy. In this area, siRNA-SQ NPs are promising new potential drug candidates with wide therapeutic applications thanks to their high colloidal stability.

## 6. Credit author statement

M.C. designed and performed the experiments and wrote the manuscript, F.G. contributed and performed the experiments of SAXS and SANS studies, M.H. developed the Fluorescence quenching experiments, S.B. contributed to the synthesis and characterization of the siRNA-SQ NPs, P.G. contributed to study design and discussion, D.D developed the azido-squalene synthesis, P.C. contribute on the discussion of the results and to the writing of the manuscript, F.W. and I.G. performed with MC and FG the SRCD experiments, F.T. contributed and performed the experiments of SAXS and SANS studies and, L.M. is the PI of the study, she supervised, designed the study and contributed to the writing of the manuscript.

## 7. Declaration of Competing Interest

The authors declare that they have no known competing financial interests or personal relationships that could have appeared to influence the work reported in this paper.

## 8. Acknowledgment

This paper is dedicated to Ms. Isabelle Grillo† (Institut Laue Langevin, 71 avenue des Martyrs, B.P. 156, 38042 Grenoble Cedex 9, France) who passed away. Ms Grillo performed the SRCD experiments.

We thank for Julien Loisel Duwattez and Alexandre Rodrigues for their technical assistance, David Carrière for SAXS-WAXS measurements performed on the SWING beamline (SOLEIL Synchrotron) during the BAG 20181790 and 20201118. SRCD experiments were performed on the DISCO Beamline at the SOLEIL Synchrotron (Saint Aubin, France). This work benefited from the use of the SasView application (http://www.sasview.org), originally developed under NSF award DMR-0520547. SasView contains code developed with funding from the European Union's Horizon 2020 research and innovation program under the SINE2020 project, grant agreement no. 654000.

The authors also thank Ghislaine Frebourg for Cryo-TEM observations (Electronic Microscopy Platform, IBPS/Institut de Biologie Paris-Seine, Université P. et M. Curie, Paris, France) and John S. Lomas (Interfaces, Traitements, Organisation et DYnamique des Systèmes (ITODYS), UFR de Chimie 75013 Paris, France) for the English editing. Marie Caillaud is grateful for the financial support of the Ile-de-France region within the framework of the "ARDoC" program (doctoral grants in targeted fields) during her doctoral fellowship.

# 9. References


Aggarwal, P., J. B. Hall, C. B. McLeland, M. A. Dobrovolskaia and S. E. McNeil (2009). "Nanoparticle interaction with plasma proteins as it relates to particle biodistribution, biocompatibility and therapeutic efficacy." Adv Drug Deliv Rev **61**(6): 428-437.

Ali, H. M., A. Maksimenko, G. Urbinati, H. Chapuis, M. Raouane, D. Desmaele, H. Yasuhiro, H. Harashima, P. Couvreur and L. Massaad-Massade (2014). "Effects of silencing the RET/PTC1 oncogene in papillary thyroid carcinoma by siRNA-squalene nanoparticles with and without fusogenic companion GALA-cholesterol." Thyroid **24**(2): 327-338.

Ali, H. M., G. Urbinati, H. Chapuis, D. Desmaele, J. R. Bertrand, P. Couvreur and L. Massaad-Massade (2014). "Effects of siRNA on RET/PTC3 junction oncogene in papillary thyroid carcinoma: from molecular and cellular studies to preclinical investigations." PLoS One **9**(4): e95964.

Ali, H. M., G. Urbinati, M. Raouane and L. Massaad-Massade (2012). "Significance and applications of nanoparticles in siRNA delivery for cancer therapy." Expert Rev Clin Pharmacol **5**(4): 403-412.

Ambike, A., V. Rosilio, B. Stella, S. Lepêtre-Mouelhi and P. Couvreur (2011). "Interaction of self-assembled squalenoyl gemcitabine nanoparticles with phospholipid-cholesterol monolayers mimicking a biomembrane." Langmuir **27**(8): 4891-4899.

Bertrand, J. R., C. Lucas, N. M. Pham, C. Durieu, P. Couvreur, C. P. Malvy and D. Desmaele (2015). "Turning Squalene into Cationic Lipid Allows a Delivery of siRNA in Cultured Cells." Nucleic Acid Ther **25**(3): 121-129.

Bilati, U., E. Allémann and E. Doelker (2005). "Development of a nanoprecipitation method intended for the entrapment of hydrophilic drugs into nanoparticles." Eur J Pharm Sci **24**(1): 67-75.

Boutary, S., M. Caillaud, M. El Madani, J.-M. Vallat, J. Loisel-Duwattez, A. Rouyer, L. Richard, C. Gracia, G. Urbinati, D. Desmaële, A. Echaniz-Laguna, D. Adams, P. Couvreur, M. Schumacher, C. Massaad and L. Massaad-Massade (2021). "Squalenoyl siRNA PMP22 nanoparticles are effective in treating mouse models of Charcot-Marie-Tooth disease type 1 A." Communications Biology **4**(1): 317.

Boutary, S., M. Caillaud, M. El Madani, J. M. Vallat, J. Loisel-Duwattez, A. Rouyer, L. Richard, C. Gracia, G. Urbinati, D. Desmaële, A. Echaniz-Laguna, D. Adams, P. Couvreur, M. Schumacher, C. Massaad and L. Massaad-Massade (2021). "Squalenoyl siRNA PMP22 nanoparticles are effective in treating mouse models of Charcot-Marie-Tooth disease type 1 A." Commun Biol **4**(1): 317.

Caillaud, M., M. El Madani and L. Massaad-Massade (2020). "Small interfering RNA from the lab discovery to patients' recovery." J Control Release **321**: 616-628.

Chaudhary, J., J. Bower and I. R. Corbin (2019). "Lipoprotein Drug Delivery Vehicles for Cancer: Rationale and Reason." Int J Mol Sci **20**(24).

Couvreur, P., L. H. Reddy, S. Mangenot, J. H. Poupaert, D. Desmaele, S. Lepetre-Mouelhi, B. Pili, C. Bourgaux, H. Amenitsch and M. Ollivon (2008). "Discovery of new hexagonal supramolecular nanostructures formed by squalenoylation of an anticancer nucleoside analogue." Small **4**(2): 247-253.

Couvreur, P., B. Stella, L. H. Reddy, H. Hillaireau, C. Dubernet, D. Desmaële, S. Lepêtre-Mouelhi, F. Rocco, N. Dereuddre-Bosquet, P. Clayette, V. Rosilio, V. Marsaud, J.-M. Renoir and L. Cattel (2006). "Squalenoyl Nanomedicines as Potential Therapeutics." Nano Letters **6**(11): 2544-2548.

Desmaele, D., R. Gref and P. Couvreur (2012). "Squalenoylation: a generic platform for nanoparticular drug delivery." J Control Release **161**(2): 609-618.

Dormont, F., M. Rouquette, C. Mahatsekake, F. Gobeaux, A. Peramo, R. Brusini, S. Calet, F. Testard, S. Lepetre-Mouelhi, D. Desmaële, M. Varna and P. Couvreur (2019). "Translation of nanomedicines from lab to industrial scale synthesis: The case of squalene-adenosine nanoparticles." J Control Release **307**: 302-314.

Elbashir, S. M. (2001). "RNA interference is mediated by 21- and 22-nucleotide RNAs." Genes & Development **15**(2): 188-200.

879 Elbashir, S. M., J. Martinez, A. Patkaniowska, W. Lendeckel and T. Tuschl (2001). "Functional anatomy
880 of siRNAs for mediating efficient RNAi in Drosophila melanogaster embryo lysate." Embo j **20**(23):
881 6877-6888.
882 Fire, A., S. Xu, M. K. Montgomery, S. A. Kostas, S. E. Driver and C. C. Mello (1998). "Potent and
883 specific genetic interference by double-stranded RNA in Caenorhabditis elegans." Nature **391**(6669):
884 806-811.
885 Gao, H. and Q. He (2014). "The interaction of nanoparticles with plasma proteins and the consequent
886 influence on nanoparticles behavior." Expert Opin Drug Deliv **11**(3): 409-420.
887 Gobeaux, F., J. Bizeau, F. Samson, L. Marichal, I. Grillo, F. Wien, S. O. Yesylevsky, C. Ramseyer, M.
888 Rouquette, S. Lepêtre-Mouelhi, D. Desmaële, P. Couvreur, P. Guenoun, J. P. Renault and F. Testard
889 (2020). "Albumin-driven disassembly of lipidic nanoparticles: the specific case of the squalene-
890 adenosine nanodrug." Nanoscale **12**(4): 2793-2809.
891 Guinier, A., G. Fournet and K. L. Yudowitch (1955). "Small-angle scattering of X-rays."
892 Gunawan, C., M. Lim, C. P. Marquis and R. Amal (2014). "Nanoparticle-protein corona complexes
893 govern the biological fates and functions of nanoparticles." J Mater Chem B **2**(15): 2060-2083.
894 Hoogenboezem, E. N. and C. L. Duvall (2018). "Harnessing albumin as a carrier for cancer therapies."
895 Adv Drug Deliv Rev **130**: 73-89.
896 Kanasty, R., J. R. Dorkin, A. Vegas and D. Anderson (2013). "Delivery materials for siRNA
897 therapeutics." Nature Materials **12**: 967.
898 Kang, M., H. Kim and C. Leal (2016). "Self-organization of Nucleic Acids in Lipid Constructs." Curr Opin
899 Colloid Interface Sci **26**: 58-65.
900 Kratz, F. (2008). "Albumin as a drug carrier: design of prodrugs, drug conjugates and nanoparticles." J
901 Control Release **132**(3): 171-183.
902 Lamichhane, S. and S. Lee (2020). "Albumin nanoscience: homing nanotechnology enabling targeted
903 drug delivery and therapy." Arch Pharm Res **43**(1): 118-133.
904 Lepeltier, E., C. Bourgaux and P. Couvreur (2014). "Nanoprecipitation and the "Ouzo effect":
905 Application to drug delivery devices." Adv Drug Deliv Rev **71**: 86-97.
906 Lepeltier, E., C. Bourgaux, A. Maksimenko, F. Meneau, V. Rosilio, E. Sliwinski, F. Zouhiri, D. Desmaële
907 and P. Couvreur (2014). "Self-assembly of polyisoprenoyl gemcitabine conjugates: influence of
908 supramolecular organization on their biological activity." Langmuir **30**(22): 6348-6357.
909 Lesniak, A., F. Fenaroli, M. P. Monopoli, C. Åberg, K. A. Dawson and A. Salvati (2012). "Effects of the
910 presence or absence of a protein corona on silica nanoparticle uptake and impact on cells." ACS Nano
911 **6**(7): 5845-5857.
912 Mariam, J., S. Sivakami and P. M. Dongre (2016). "Albumin corona on nanoparticles - a strategic
913 approach in drug delivery." Drug Deliv **23**(8): 2668-2676.
914 Marichal, L., J. Degrouard, A. Gatin, N. Raffray, J. C. Aude, Y. Boulard, S. Combet, F. Cousin, S.
915 Hourdez, J. Mary, J. P. Renault and S. Pin (2020). "From Protein Corona to Colloidal Self-Assembly:
916 The Importance of Protein Size in Protein-Nanoparticle Interactions." Langmuir **36**(28): 8218-8230.
917 Marichal, L., G. Giraudon-Colas, F. Cousin, A. Thill, J. Labarre, Y. Boulard, J. C. Aude, S. Pin and J. P.
918 Renault (2019). "Protein-Nanoparticle Interactions: What Are the Protein-Corona Thickness and
919 Organization?" Langmuir **35**(33): 10831-10837.
920 Massaad-Massade, L., S. Boutary, M. Caillaud, C. Gracia, B. Parola, S. B. Gnaouiya, B. Stella, S. Arpicco,
921 E. Buchy, D. Desmaele, P. Couvreur and G. Urbinati (2018). "New Formulation for the Delivery of
922 Oligonucleotides Using "Clickable" siRNA-Polyisoprenoid-Conjugated Nanoparticles: Application to
923 Cancers Harboring Fusion Oncogenes." Bioconjug Chem **29**(6): 1961-1972.
924 Miles, A. J. and B. A. Wallace (2018). "CDtoolX, a downloadable software package for processing and
925 analyses of circular dichroism spectroscopic data." Protein Science **27**(9): 1717-1722.
926 Monopoli, M. P., C. Aberg, A. Salvati and K. A. Dawson (2012). "Biomolecular coronas provide the
927 biological identity of nanosized materials." Nat Nanotechnol **7**(12): 779-786.
928 Ogawara, K., K. Furumoto, S. Nagayama, K. Minato, K. Higaki, T. Kai and T. Kimura (2004). "Pre-
929 coating with serum albumin reduces receptor-mediated hepatic disposition of polystyrene
930 nanosphere: implications for rational design of nanoparticles." J Control Release **100**(3): 451-455.

Ozpolat, B., A. K. Sood and G. Lopez-Berestein (2014). "Liposomal siRNA nanocarriers for cancer therapy." Adv Drug Deliv Rev **66**: 110-116.
Raouane, M., D. Desmaele, M. Gilbert-Sirieix, C. Gueutin, F. Zouhiri, C. Bourgaux, E. Lepeltier, R. Gref, R. Ben Salah, G. Clayman, L. Massaad-Massade and P. Couvreur (2011). "Synthesis, characterization, and in vivo delivery of siRNA-squalene nanoparticles targeting fusion oncogene in papillary thyroid carcinoma." J Med Chem **54**(12): 4067-4076.
Richard, D., M. Ferrand and G. Kearley (1996). "Analysis and visualisation of neutron-scattering data." Journal of Neutron Research **4**(1-4): 33-39.
Ristori, S., L. Ciani, G. Candiani, C. Battistini, A. Frati, I. Grillo and M. In (2012). "Complexing a small interfering RNA with divalent cationic surfactants." Soft Matter **8**(3): 749-756.
Rouquette, M., K. Ser-Le Roux, M. Polrot, C. Bourgaux, J. P. Michel, F. Testard, F. Gobeaux and S. Lepetre-Mouelhi (2019). "Towards a clinical application of freeze-dried squalene-based nanomedicines." J Drug Target **27**(5-6): 699-708.
Saha, D., F. Testard, I. Grillo, F. Zouhiri, D. Desmaele, A. Radulescu, S. Desert, A. Brulet, P. Couvreur and O. Spalla (2015). "The role of solvent swelling in the self-assembly of squalene based nanomedicines." Soft Matter **11**(21): 4173-4179.
Schumaker, V. N. and G. H. Adams (1969). "Circulating lipoproteins." Annu Rev Biochem **38**: 113-136.
Sleep, D. (2015). "Albumin and its application in drug delivery." Expert Opin Drug Deliv **12**(5): 793-812.
Sobot, D., S. Mura, M. Rouquette, B. Vukosavljevic, F. Cayre, E. Buchy, G. Pieters, S. Garcia-Argote, M. Windbergs, D. Desmaele and P. Couvreur (2017). "Circulating Lipoproteins: A Trojan Horse Guiding Squalenoylated Drugs to LDL-Accumulating Cancer Cells." Mol Ther **25**(7): 1596-1605.
Sobot, D., S. Mura, S. O. Yesylevskyy, L. Dalbin, F. Cayre, G. Bort, J. Mougin, D. Desmaele, S. Lepetre-Mouelhi, G. Pieters, B. Andreiuk, A. S. Klymchenko, J. L. Paul, C. Ramseyer and P. Couvreur (2017). "Conjugation of squalene to gemcitabine as unique approach exploiting endogenous lipoproteins for drug delivery." Nat Commun **8**: 15678.
Tatiparti, K., S. Sau, S. K. Kashaw and A. K. Iyer (2017). "siRNA Delivery Strategies: A Comprehensive Review of Recent Developments." Nanomaterials (Basel) **7**(4).
Thompson, J. D., D. J. Kornbrust, J. W. Foy, E. C. Solano, D. J. Schneider, E. Feinstein, B. A. Molitoris and S. Erlich (2012). "Toxicological and pharmacokinetic properties of chemically modified siRNAs targeting p53 RNA following intravenous administration." Nucleic Acid Ther **22**(4): 255-264.
Tuschl, T. (2002). Expanding small RNA interference. Nat Biotechnol. United States. **20:** 446-448.
Urbinati, G., H. M. Ali, Q. Rousseau, H. Chapuis, D. Desmaele, P. Couvreur and L. Massaad-Massade (2015). "Antineoplastic Effects of siRNA against TMPRSS2-ERG Junction Oncogene in Prostate Cancer." PLoS One **10**(5): e0125277.
Urbinati, G., H. M. Ali, Q. Rousseau, H. Chapuis, D. Desmaele, P. Couvreur and L. Massaad-Massade (2015). "Antineoplastic Effects of siRNA against TMPRSS2-ERG Junction Oncogene in Prostate Cancer." Plos One **10**(5): 23.
Urbinati, G., I. de Waziers, M. Slamic, T. Foussigniere, H. M. Ali, D. Desmaele, P. Couvreur and L. Massaad-Massade (2016). "Knocking Down TMPRSS2-ERG Fusion Oncogene by siRNA Could be an Alternative Treatment to Flutamide." Mol Ther Nucleic Acids **5**: e301.
Urbinati, G., I. de Waziers, M. Slamic, T. Foussigniere, H. M. Ali, D. Desmaele, P. Couvreur and L. Massaad-Massade (2016). "Knocking Down TMPRSS2-ERG Fusion Oncogene by siRNA Could be an Alternative Treatment to Flutamide." Molecular Therapy-Nucleic Acids **5**: 12.
Urbinati, G., A. M. Hafiz and L. Massaad-Massade (2013). "New pharmacological approach by siRNA against junction oncogenes for thyroid and prostate cancers." International Journal of Molecular Medicine **32**: S37-S37.
Wasan, K. M., D. R. Brocks, S. D. Lee, K. Sachs-Barrable and S. J. Thornton (2008). "Impact of lipoproteins on the biological activity and disposition of hydrophobic drugs: implications for drug discovery." Nat Rev Drug Discov **7**(1): 84-99.
Weis, J., K. G. Claeys, A. Roos, H. Azzedine, I. Katona, J. M. Schröder and J. Senderek (2017). "Towards a functional pathology of hereditary neuropathies." Acta Neuropathol **133**(4): 493-515.

983 Whitehead, K. A., R. Langer and D. G. Anderson (2009). "Knocking down barriers: advances in siRNA
984 delivery." Nat Rev Drug Discov **8**(2): 129-138.
985 Wolfrum, C., S. Shi, K. N. Jayaprakash, M. Jayaraman, G. Wang, R. K. Pandey, K. G. Rajeev, T.
986 Nakayama, K. Charrise, E. M. Ndungo, T. Zimmermann, V. Koteliansky, M. Manoharan and M. Stoffel
987 (2007). "Mechanisms and optimization of in vivo delivery of lipophilic siRNAs." Nat Biotechnol **25**(10):
988 1149-1157.
989 Yesylevskyy, S. O., C. Ramseyer, M. Savenko, S. Mura and P. Couvreur (2018). "Low-Density
990 Lipoproteins and Human Serum Albumin as Carriers of Squalenoylated Drugs: Insights from
991 Molecular Simulations." Mol Pharm **15**(2): 585-591.
992 Zhou, Y., H. Bazick, J. R. Miles, A. I. Fethiere, M. O. Al Salihi, S. Fazio, H. Tavori and L. Notterpek
993 (2019). "A neutral lipid-enriched diet improves myelination and alleviates peripheral nerve pathology
994 in neuropathic mice." Experimental neurology **321**: 113031.
995
996

# Appendix A. Supplementary material

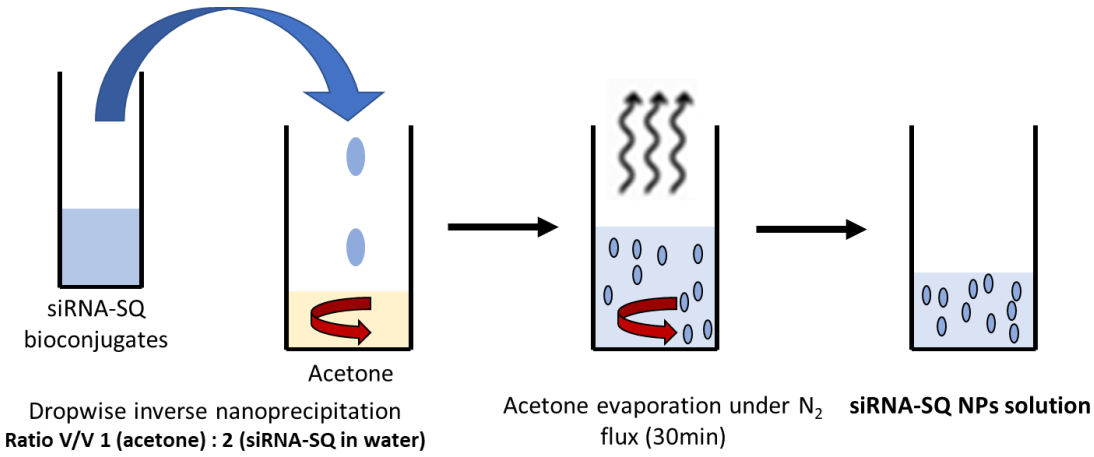


Figure S1: Sketch of siRNA-SQ nanoparticles preparation**.** The siRNA-SQ bioconjugates were obtained after Cu-free click chemistry and annealing to the antisense strand. Then, the siRNA-SQ NPs were prepared by inverse nanoprecipitation : siRNA-SQ bioconjugates in water were added drop wisely to a stirred organic phase (acetone) with a volume/volume ratio of 1 [organic phase, acetone]: 2 [aqueous phase, siRNA-SQ bioconjugate]. Then acetone was evaporated using nitrogen (N2) flux to obtain an aqueous suspension of pure siRNA-SQ NPs.

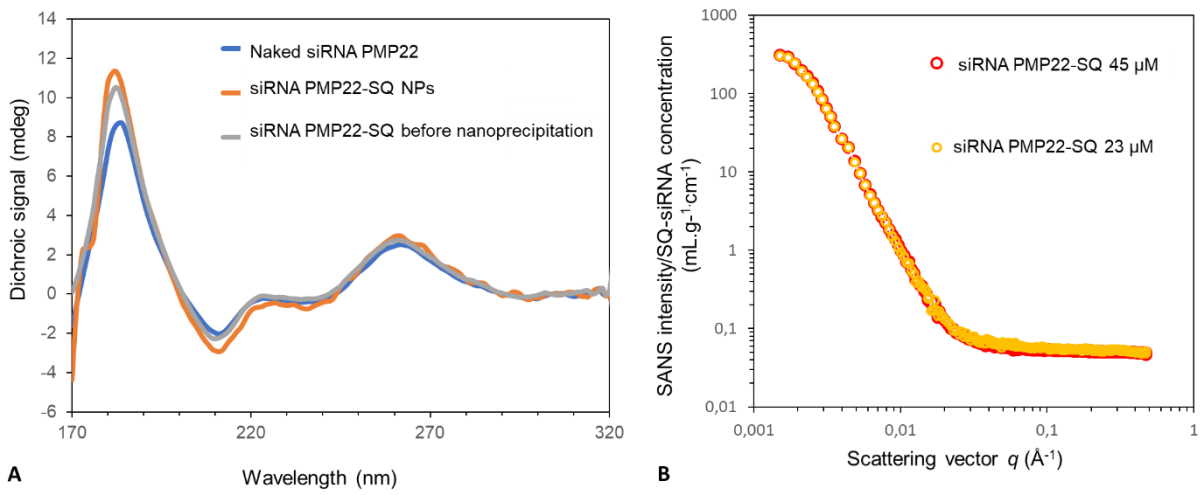


Figure S2: Circular dichroism spectrum of siRNA. **A)** Naked siRNA (blue curve); siRNA-SQ NPs (orange) siRNA-SQ bioconjugates before nanoprecipitation (grey). Intensity difference (y-axis) is due to the use of different sample concentrations. **B)** Small-angle neutron scattering patterns of two dilutions of siRNA-SQ suspensions. Red circles: 45 µM; yellow circles: 23 µM. The small-angle region corresponds to values of $q < 0.002$ Å$^{-1}$, mean angles 0.002 to 0.04 Å$^{-1}$ and the large-angle $q > 0.04$ Å$^{-1}$.

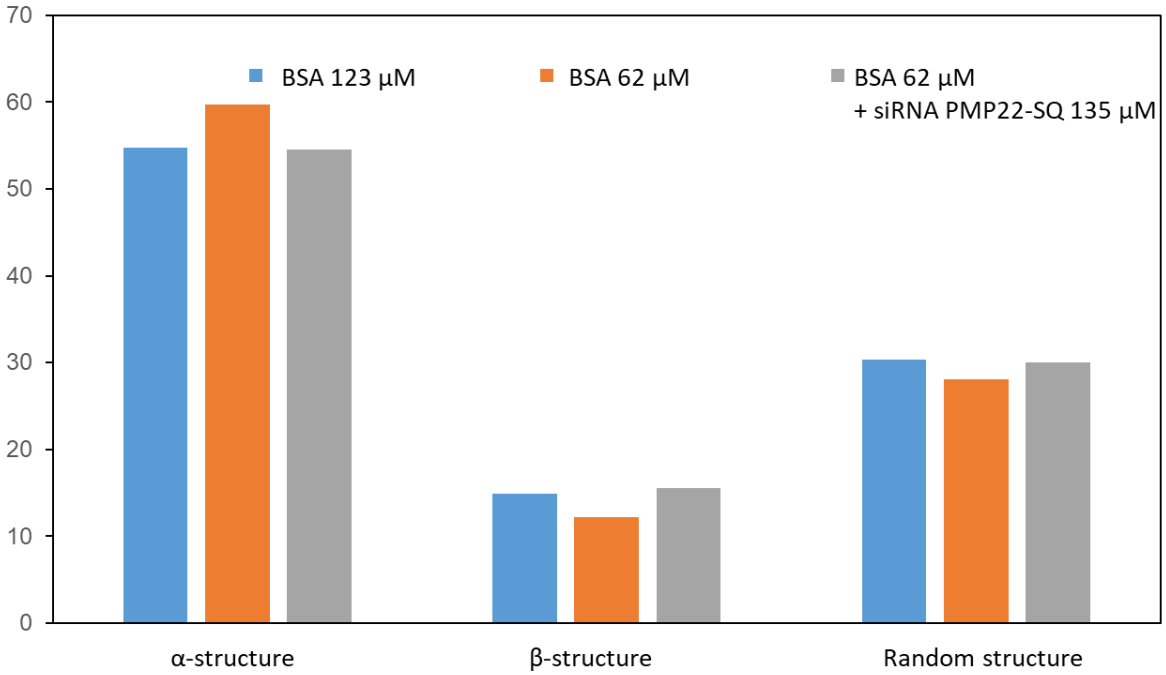


Figure S3: Quantification of the secondary structure of BSA. After circular dichroism analysis, quantifications of BSA were performed by BestSel program (http://bestsel.elte.hu/index.php). The histogram represents the comparison of two BSA concentrations (123 µM in blue and 62 µM in orange) alone or in presence of siRNA-SQ NPs (in grey) with BSA at 62 µM. No difference was observed for the different conditions.

**Table S1:** Table comparing siRNA size estimation

| **"Source"** | **Dimensions (nm)** |
|---|---|
| **22 base pairs x 3.5 Å** | L = 7 nm |
| **SANS pattern Ristori *et al.*** | Cylindrical form factor<br>L = 5.2 nm<br>R = 1.1 nm |
| **SAXS pattern of siRNA strands** | Cylindrical form factor<br>L = 7 nm<br>R = 1.1 nm |
| **SAXS pattern of siRNA-SQ** | Cylindrical form factor<br>L = 4 nm<br>R = 1.1 nm |

The scattering pattern originating from the naked siRNA PMP22 dispersion exhibited an oscillation in the same *q*-range in accordance with the SANS analysis of similar siRNA strands reported by Ristori *et al.* (Ristori, Ciani et al. 2012).

**Supplementary information, equation A**

$$\frac{F_0}{F} = 1 + K_{sv}[\text{siRNA PMP22-SQ}] = 1 + K_q\tau_0[\text{siRNA PMP22-SQ}]$$

**Equation A. Stern-Volmer equation**: $F_0$ and F are fluorescence intensities of BSA in absence and presence of quencher (siRNA-SQ NPs), [siRNA PMP22-SQ] the molar concentration of siRNA PMP22-SQ (in M), $K_{sv}$ ($M^{-1}$) the Stern-Volmer constant which depends on $K_q$ ($M^{-1}.s^{-1}$) and $\tau_0$ (s) the average lifetime of tryptophan fluorescence in the absence of quencher, equals $10^{-8}$ s.

**Supplementary information, equation B**

Interaction between the siRNA-SQ nanoparticles (NPs) and BSA can be probed in the following formula:

(B1) $\text{siRNAPMP22-SQ NPs} + n(\text{BSA}) \leftrightarrow [\text{ siRNA PMP22-SQ NPs-}(\text{BSA})_n]$

According to this equation we can determine the apparent dissociation constant ($K_{obs}$) at pH 7 and at 25°C.

(B2) $$K_{obs} = \frac{[\text{siRNA PMP22-SQ}][\text{BSA}]}{[\text{siRNA PMP22-SQ-(BSA)}]}$$

Based on equation (1), the intrinsic fluorescence intensity of the mixture is expressed as a function of the concentrations of all species in solution, weighted by experimental factors $f_1$, $f_2$ and $f_3$ for [siRNA PMP22-SQ], [BSA] and |siRNA PMP22-SQ-BSA] respectively:

(B3) $$F = f_1[\text{siRNA PMP22-SQ}] + f_2[\text{BSA}] + f_3[\text{siRNA PMP22-SQ-}(\text{BSA})_n]$$

In absence of BSA, the initial fluorescence intensity is given by: $F_0 = f_1[\text{siRNA PMP22-SQ}]_{initial}$

The experimental conditions are as follow: 1) ratio [BSA]: [siRNA-SQ] < 1; 2) the fluorescence intensity emitted by the siRNA PMP22-SQ NPs + BSA mixture should be completely adsorbed BSA, therefore 3) the intensity emitted from free BSA ($f_2$|BSA]) can be neglected.

The experimental factor $f_3$ is calculated based on raw data. From the variation in fluorescence emission $\Delta F = F - F_0$ of equation **(3)** the $K_{obs}$ **(2)** can be calculated from the linear least-squares regression:

(B4) $$\frac{f_3 - f_1}{\Delta F} = \frac{1}{[\text{siRNA PMP22-SQ}]_{initial}} + \frac{K_{obs}}{[\text{siRNA PMP22-SQ}]_{initial}\left([\text{BSA}] - \frac{\Delta F}{f_3 - f_1}\right)}$$

**Supplementary information, equation C**

1) Mass calculation of one nanoparticle

As serum components will interact with the squalene moiety which surround the nanoparticle, we postulated that the mass of one nanoparticle is based on its density ($\rho_{SQ}$ = 858 kg/m$^3$) and the nanoparticle volume:

(C1) $$m_{NP} = \rho_{SQ} V_{NP}$$

Number of NPs can be calculated as follow:

(C2) $$N_{NP} = \frac{C_m(\text{siRNA PMP22-SQ})}{m_{NP}}$$

2) Determination of the number of proteins

Based on electrophoresis experimental conditions and molecular weight of the BSA, we can calculate the total mass of BSA:

(C3) $$m_{\text{total BSA}} = [BSA] MM_{BSA} V$$

Where [BSA] is the molar concentration of BSA, $MM_{BSA}$ the BSA molecular weight (65,000 g/mol) and V the volume used for incubation before electrophoresis.

Number of BSA proteins can be determined as follow:

(C4) $$N_{BSA} = \frac{m_{\text{total BSA}}}{MM_{BSA}} \mathcal{N}_A$$

Where N is the BSA protein number and $\mathcal{N}_A$ the Avogadro number (number of elementary entities contained in a mole of matter, equal to 6.023 x 10$^{23}$).

3) Determination of BSA proteins per nanoparticle

Based on (2) and (4), we can calculate the number of BSA interacting with one nanoparticle:

(C5) $$\text{Number } {}^{BSA}/_{NP} = \frac{N_{BSA}}{m_{NP}}$$